Eur. Phys. J. A **8**, 455–479 (2000)

THE EUROPEAN PHYSICAL JOURNAL A

Real and virtual Compton scattering off the nucleon

M. Vanderhaeghen[a]

Institut für Kernphysik, Johannes Gutenberg-Universität, D-55099 Mainz, Germany

Received: 4 August 2000
Communicated by A. Schäfer

Abstract. A review is given of the very recent developments in the fields of real and virtual Compton scattering off the nucleon. Both real and virtual Compton scattering reactions are discussed at low outgoing photon energy where one accesses polarizabilities of the nucleon. The real Compton scattering at large momentum transfer is discussed which is asymptotically a tool to obtain information on the valence quark wave function of the nucleon. The rapid developments in deeply virtual Compton scattering and associated meson electroproduction reactions at high energy, high photon virtuality and small momentum transfer to the nucleon are discussed. A unified theoretical description of those processes has emerged over the last few years, which gives access to new, generalized parton distributions. The experimental status and perspectives in these fields are also discussed.

PACS. 13.60.Fz Elastic and Compton scattering – 13.40.-f Electromagnetic processes and properties – 12.38.Bx Perturbative calculations

1 Introduction

In the study of hadron structure, one of the main questions is how hadrons and nuclei are built from quarks and gluons and how one goes over from a description in terms of quark and gluon degrees of freedom to a description in terms of hadronic degrees of freedom.

Nowadays, precision experiments at high energy have established Quantum Chromo Dynamics (QCD) as the gauge theory of strong interactions describing the dynamics between colored quarks and gluons. QCD exhibits the property that the interaction between the quarks becomes weak at very short distances, which is known as asymptotic freedom, and which allows us to use perturbation theory to describe high-energy strong interaction phenomena. On the other hand at low energy, the QCD coupling constant grows, and quarks and gluons are confined into colorless mesons and baryons, which are the particles as seen through experiments. In this phase of hadronic matter, the underlying chiral symmetry of QCD, due to the nearly massless up, down and approximately also strange quarks, is spontaneously broken. To describe this regime directly from the QCD Lagrangian is a hard task which still defies a solution due to the strong coupling constant requiring non-perturbative methods. Probably the most promising and direct approach is the numerical solution of QCD through lattice calculations. For static hadronic properties, such as, *e.g.*, masses, much progress has already been made, but for more complicated hadron structure quantities, such as *e.g.*, nucleon parton distributions, lattice calculations are still in their infancy.

In absence of a full numerical solution of QCD, which would be able to describe the rich complexity of the hadronic many body systems from their underlying dynamics, a complementary strategy to refine our understanding of hadron structure is to perform new types of precision experiments in kinematical regimes at low energy, which require an inherent non-perturbative description. Besides, one may perform new types of experiments at high energies, in those kinematical regimes where factorization theorems have been proven. Such experiments will allow us to use an accurate perturbative QCD description of the reaction dynamics as a tool to extract new types of non-perturbative hadron structure information.

In this quest at the intersection of particle and nuclear physics, the experiments performed with electromagnetic probes play an important role. A new generation of precision experiments has become possible with the advent of the new electron accelerators and in combination with high-precision and large acceptance detectors. In particular, high precision Compton scattering experiments have become a reality in recent years. In Compton scattering, a real or virtual photon interacts with the nucleon and a real photon is emitted in the process. As this is a purely electromagnetic process, it yields small cross-sections (compared to hadronic reactions), but on the other hand constitutes a clean probe of hadron structure.

In this paper, a review will be given of very recent developments in the field of real and virtual Compton scattering off the nucleon. I shall discuss real and virtual Compton scattering at the same time and point

---

[a] e-mail: `marcvdh@kph.uni-mainz.de`

out their complementarity and the differences in the extracted nucleon structure information. The emphasis is on those kinematical regimes where a fruitful interpretation is terms of nucleon structure observables has been shown to be possible. Virtual Compton scattering (VCS) off the nucleon has been reviewed before in ref. [1], which is referred to for most technical details. For the VCS part, the emphasis is on the progress over the past two years in the light of the first high precision VCS data in the threshold regime now available, and on the rapid development in the field of deeply virtual Compton scattering (DVCS) at large photon virtuality.

In section 2, the real Compton scattering (RCS) process below pion threshold is discussed. In this regime, the RCS process can be interpreted as the global response of the nucleon to an applied electromagnetic field, which allows us to access global nucleon polarizabilities. A dispersion relation formalism is described, which was developed as a method to minimize the model uncertainty in the extraction of nucleon polarizabilites from both unpolarized and polarized RCS data at low energy.

In section 3, the virtual Compton scattering (VCS) reaction at low energy is discussed. It consists of a generalization of RCS in which both energy and momentum of the virtual photon can be varied independently, which allows us to extract response functions, parametrized by the so-called generalized polarizabilities (GP's) of the nucleon. A first dedicated VCS experiment was performed at the MAMI accelerator, and two combinations of those GP's have been measured. Their values are compared with nucleon structure model predictions. Further experimental programs are underway at the major electron accelerators to measure the VCS observables. It is outlined how results of such experiments can be interpreted in terms of the nucleon GP's, and in particular how polarization observables can separate the different GP's.

Besides the low-energy region, RCS at high energy and large momentum transfer is a tool to access information on the partonic structure of the nucleon. In section 4, a leading-order perturbative QCD calculation of RCS is described, which was developed to extract the valence quark wave function of the nucleon. Such an approach is compared with competing mechanisms, and it is pointed out how the planned experiments can shed light on this field.

Section 5 discusses the recent developments in deeply virtual Compton scattering (DVCS) and associated meson electroproduction reactions at high energy, high photon virtuality Q^2 and small momentum transfer to the nucleon. It is shown how a unified theoretical description of those processes has recently emerged and how it gives access to new parton distributions, the so-called skewed parton distributions, which are generalizations of the usual parton distributions as known from inclusive deep inelastic lepton scattering. Leading-order perturbative QCD calculations of DVCS and different meson electroproduction reactions, using an ansatz for the skewed parton distributions, are discussed in the kinematical regimes accessible at present or planned facilities. The corrections to those leading-order QCD amplitudes and further open questions in this field are touched on briefly.

In section 6, the calculation of the QED radiative corrections to the VCS process is discussed, which is indispensable to accurately extract the nucleon structure information from VCS experiments.

Finally, the conclusions and perspectives are given in section 7.

2 Real Compton scattering (RCS) and nucleon polarizabilities

2.1 Introduction

In the study of nucleon structure, real Compton scattering (RCS) at low energy is a precision tool to access global information on the nucleon ground state and its excitation spectrum. RCS off the nucleon is determined by 6 independent helicity amplitudes, which are functions of two variables, *e.g.*, the Lorentz invariant variables ν (related to the *lab* energy of the incident photon) and t (related to the momentum transfer to the target). In the limit $\nu \to 0$, corresponding to wavelengths much larger than the nucleon size, the general structure of these amplitudes is governed by low-energy theorems (LET) based on Lorentz invariance, gauge invariance and crossing symmetry. These theorems predict that the leading terms of an expansion in ν are determined by global properties of the nucleon, *i.e.* its charge, mass and anomalous magnetic moment. Furthermore, the internal structure shows up only at relative order ν^2 and can be parametrized in terms of the polarizabilities. In this way, there appear 6 polarizabilities for the nucleon, the electric and magnetic (scalar) polarizabilities α and β respectively, familiar from classical physics, and 4 spin (vector) polarizabilities γ_1 to γ_4, originating from the spin-1/2 nature of the nucleon. These polarizabilities describe the response of the nucleon's charge, magnetization, and spin distributions to an external quasistatic electromagnetic field. As such the polarizabilities are fundamental structure constants of the composite system.

The differential cross-section for RCS in the limit $\nu \to 0$ is given by the (model independent) Thomson term, as a consequence of the LET. The electric and magnetic polarizabilities then appear, in a low-energy expansion for RCS, as interference between the Thomson term and the subleading terms, *i.e.* as contribution of $O(\nu^2)$ in the differential cross-section. In this way, α and β can in principle be separated by studying the RCS angular distributions. However, it has never been possible to isolate this term and thus to determine the polarizabilities in a model independent way. The obvious reason is that, for sufficiently small energies, say $\nu \leq 40$ MeV, the structure effects are extremely small and hence the statistical errors for the polarizabilities large. Therefore, one has to go to larger energies, where the higher terms in the expansion become increasingly important and where also the spin polarizabilities come into play. To determine the nucleon polarizabilities from RCS observables, a reliable estimate of higher terms in the energy is therefore of utmost importance. To this end, actual experiments were usually analyzed in an unsubtracted dispersion relation formalism at fixed t [2]. Using such an analysis, the proton scalar polarizabilities were derived from Compton scattering data below pion threshold, with the results [3]

$$\begin{aligned}\alpha &= (12.1 \pm 0.8 \pm 0.5) \times 10^{-4}\,\mathrm{fm}^3 \,, \\ \beta &= (2.1 \mp 0.8 \mp 0.5) \times 10^{-4}\,\mathrm{fm}^3 \,. \end{aligned} \tag{1}$$

Very recently, new RCS data on the proton below pion threshold have become available [4]. These data increase the available world data set substantially, and yield, in an unsubtracted DR formalism, the results :

$$\begin{aligned}\alpha &= (11.89 \pm 0.57) \times 10^{-4}\,\mathrm{fm}^3 \,, \\ \beta &= (1.17 \pm 0.75) \times 10^{-4}\,\mathrm{fm}^3 \,. \end{aligned} \tag{2}$$

The sum of the scalar polarizabilities, which appears in the forward spin-averaged Compton amplitude, can be determined directly from the total photoabsorption cross-section by Baldin's sum rule [5], which yields a rather precise value :

$$\alpha + \beta = (14.2 \pm 0.5) \times 10^{-4}\,\mathrm{fm}^3 \,, \tag{3}$$

$$= (13.69 \pm 0.14) \times 10^{-4}\,\mathrm{fm}^3 \,, \tag{4}$$

with (3) from ref. [6] and (4) from ref. [7].

Similarly, the proton forward spin polarizability can be evaluated by an integral over the difference of the absorption cross-sections in states with helicity 3/2 and 1/2,

$$\gamma_0 = \gamma_1 - \gamma_2 - 2\gamma_4 = -1.34 \times 10^{-4}\,\mathrm{fm}^4 \,, \tag{5}$$

$$= -0.80 \times 10^{-4}\,\mathrm{fm}^4 \,, \tag{6}$$

with (5) from ref. [8] and (6) from ref. [9]. While the predictions of eqs. (5,6) rely on pion photoproduction multipoles, the helicity cross-sections have now been directly determined at MAMI by scattering photons with circular polarizations on polarized protons [10]. The contribution to γ_0 for the proton within the measured integration range (200 MeV $\leq \nu \leq$ 800 MeV) is [10] :

$$\gamma_0 \Big|_{200\ \mathrm{MeV}}^{800\ \mathrm{MeV}} = (-1.68 \pm 0.07) \times 10^{-4}\,\mathrm{fm}^4 \,. \tag{7}$$

The contribution below 200 MeV can be estimated with the HDT pion photoproduction multipoles [11] to yield +1.0, and an estimate of the contribution above 800 MeV based on the SAID pion photoproduction multipoles [12] yields −0.02, which results in a total value : $\gamma_0 = -0.7$ (here and in the following, all spin polarizabilities are given in units $10^{-4}\,\mathrm{fm}^4$).

Furthermore, unpolarized RCS data in the $\Delta(1232)$-region were used to give — within a dispersion relation formalism — a first prediction for the so-called backward spin polarizability of the proton, *i.e.* the particular combination $\gamma_\pi = \gamma_1 + \gamma_2 + 2\gamma_4$ entering the Compton spin-flip amplitude at $\theta = 180°$ [13] :

$$\gamma_\pi = -\left[27.1 \pm 2.2(\mathrm{stat}+\mathrm{syst}) \begin{matrix}+2.8 \\ -2.4\end{matrix}(\mathrm{model})\right] \times 10^{-4}\,\mathrm{fm}^4. \tag{8}$$

These values for the polarizabilities can be compared with our present day theoretical understanding from chiral perturbation theory (ChPT). A calculation to $O(p^4)$ in heavy baryon ChPT (HBChPT), where the expansion parameter p is an external momentum or the quark mass, yields (here and in the following, α and β are given in units $10^{-4}\,\mathrm{fm}^3$) : $\alpha = 10.5 \pm 2.0$ and $\beta = 3.5 \pm 3.6$, the errors being due to 4 counter terms entering to that order, which were estimated by resonance saturation [14]. One of these counter terms describes the large paramagnetic contribution of the $\Delta(1232)$ resonance, which is partly cancelled by large diamagnetic contributions of pion-nucleon (Nπ)-loops. In view of the importance of the Δ-resonance, the calculation was also done by including the Δ as a dynamical degree of freedom. This adds a further expansion parameter, the difference of the Δ and nucleon masses ("ϵ expansion"). A calculation to $O(\epsilon^3)$ yielded $\alpha = 12.2 + 0 + 4.2 = 16.4$ and $\beta = 1.2 + 7.2 + 0.7 = 9.1$, the 3 separate terms referring to contributions of Nπ-loops (which is the $O(p^3)$ result), Δ-pole terms, and $\Delta\pi$-loops [15,16]. These $O(\epsilon^3)$ predictions are clearly at variance with the data, in particular $\alpha + \beta = 25.5$ is nearly twice the rather precise value determined from Baldin's sum rule eq. (4).

The spin polarizabilities have also been calculated in HBChPT. The $O(\epsilon^3)$ predictions for the proton are [16] : $\gamma_0 = 4.6 - 2.4 - 0.2 + 0 = +2.0$, and $\gamma_\pi = 4.6 + 2.4 - 0.2 - 43.5 = -36.7$, the 4 separate contributions referring to Nπ-loops ($O(p^3)$ result), Δ-poles, $\Delta\pi$-loops, and the triangle anomaly, in that order. It is obvious that the anomaly or π^0-pole gives by far the most important contribution to γ_π, and that it would require surprisingly large higher-order contributions to bring γ_π close to the value of eq. (8). Recently, the Nπ-loop contribution to the spin polarizabilities have been evaluated in HBChPT to $O(p^4)$ by several groups [17–19]. In refs. [17,18], the result for the proton is $\gamma_0 = +4.5 - 8.4$, where the two contributions are the $O(p^3)$ and $O(p^4)$ Nπ-loop contributions, in this order. Based on the large $O(p^4)$ correction term, the authors in [17,18] call the convergence of the chiral expansion into question. However in ref. [19], different results were obtained for the $O(p^4)$ Nπ-loop contributions, to the 4 spin polarizabilities. It was argued that these differences are due to how one defines and extracts the $O(p^4)$ spin-dependent polarizabilities in chiral effective field theories. Following the procedure of ref. [19], which removes first all one-particle reducible contributions from the spin-dependent Compton amplitude, the resulting values for γ_0 and γ_π of the proton are $\gamma_0 = +4.6 - 5.6 = -1.0$, and $\gamma_\pi = +4.6 - 1.2 = +3.4$ (without the π^0-pole), the separate contributions being again the $O(p^3)$ and $O(p^4)$ Nπ-loop contributions, respectively. For γ_0, a convergence of HBChPT at order $O(p^4)$ was not expected [19], whereas the result for γ_π — when adding the π^0-pole contribution — is not compatible with the estimate of eq. (8) obtained by ref. [13].

In order to refine our present understanding of the nucleon polarizabilities, a better understanding of the convergence of the HBChPT expansion is absolutely necessary, and it is to be hoped that a calculation to $O(\epsilon^4)$ will clarify the status. On the other hand, it is also indispensable to minimize any model dependence in the extraction of the polarizabilities from the data. To this end, a fixed-t subtracted dispersion relation (DR) formalism was developed in ref. [9] for RCS off the nucleon at photon energies below 500 MeV, as a formalism to extract the nucleon polarizabilities with a minimum of model dependence as is described in the following.

2.2 Fixed-t subtracted dispersion relations for RCS

To perform a dispersion theoretical analysis of Compton scattering, one has to calculate the 6 independent structure functions $A_i(\nu, t)$, $i = 1, ..., 6$ (defined in ref. [2]). They are functions of the usual Mandelstam variable t, and of ν, defined in terms of the Mandelstam variables s and u as $\nu = (s-u)/(4m_{\rm N})$, with $m_{\rm N}$ the nucleon mass. The invariant amplitudes A_i are free of kinematical singularities and constraints, and because of the crossing symmetry they satisfy the relation $A_i(\nu,t) = A_i(-\nu,t)$. Assuming further analyticity and an appropriate high-energy behavior, the amplitudes A_i fulfill unsubtracted DR at fixed t :

$$\mathrm{Re}\, A_i(\nu,t) \;=\; A_i^{\rm B}(\nu,t) \;+\; \frac{2}{\pi}\,\mathcal{P}\int_{\nu_{\rm thr}}^{+\infty} \mathrm{d}\nu'\; \frac{\nu'\; \mathrm{Im}_s A_i(\nu',t)}{\nu'^2-\nu^2}\,, \tag{9}$$

where $A_i^{\rm B}$ are the Born (nucleon pole) contributions, and where $\mathrm{Im}_s A_i$ are the discontinuities across the s-channel cuts of the Compton process, starting from the threshold for pion production, $\nu_{\rm thr}$. However, such unsubtracted DR require that at high energies ($\nu \to \infty$) the amplitudes $\mathrm{Im}_s A_i(\nu,t)$ drop fast enough such that the integral of eq. (9) is convergent and the contribution from the semicircle at infinity can be neglected. For real Compton scattering, Regge theory predicts the following high-energy behavior for $\nu \to \infty$ and fixed t [2] :

$$A_{1,2} \sim \nu^{\alpha(t)}\,, \qquad A_{3,5,6} \sim \nu^{\alpha(t)-2}\,, \qquad A_4 \sim \nu^{\alpha(t)-3}\,, \tag{10}$$

where $\alpha(t) \lesssim 1$ is the Regge trajectory. Due to the high-energy behavior of eq. (10), the unsubtracted dispersion integral of eq. (9) diverges for the amplitudes A_1 and A_2. In order to obtain useful results for these two amplitudes, L'vov *et al.* [2] proposed to close the contour of the integral in eq. (9) by a semi-circle of finite radius $\nu_{\rm max}$ in the complex plane (instead of the usually assumed infinite radius!), *i.e.* the real parts of A_1 and A_2 are calculated from the decomposition

$$\mathrm{Re}\, A_i(\nu,t) \;=\; A_i^{\rm B}(\nu,t) \;+\; A_i^{\rm int}(\nu,t) \;+\; A_i^{\rm as}(\nu,t)\,, \tag{11}$$

with $A_i^{\rm int}$ the s-channel integral from pion threshold $\nu_{\rm thr}$ to a finite upper limit $\nu_{\rm max}$, and an 'asymptotic contribution' $A_i^{\rm as}$ representing the contribution along the finite semi-circle of radius $\nu_{\rm max}$ in the complex plane. In the actual calculations, the s-channel integral is typically evaluated up to a maximum photon energy of about 1.5 GeV, for which the imaginary part of the amplitudes can be expressed through unitarity by meson photoproduction amplitudes (mainly 1π and 2π photoproduction) taken from experiment. All contributions from higher energies are then absorbed in the asymptotic terms $A_i^{\rm as}$, which are replaced by a finite number of energy-independent poles in the t-channel. In particular the asymptotic part of A_1 is parametrized by the exchange of a scalar particle in the t-channel, *i.e.* an effective "σ-meson" [2]. In a similar way, the asymptotic part of A_2 is described by the π^0 t-channel pole. This procedure is relatively safe for A_2 because of the dominance of the π^0 pole or triangle anomaly, which is well established both experimentally and on general grounds as Wess-Zumino-Witten term. However, it introduces a considerable model-dependence in the case of A_1.

It was therefore the aim of ref. [9] to avoid the convergence problem of unsubtracted DR and the phenomenology necessary to determine the asymptotic contribution. To this end, it was proposed to consider DR's at fixed t that are once subtracted at $\nu = 0$,

$$\begin{aligned}\mathrm{Re}\, A_i(\nu,t) \;&=\; A_i^{\rm B}(\nu,t) \;+\; \left[A_i(0,t) - A_i^{\rm B}(0,t)\right] \\ &+\; \frac{2}{\pi}\,\nu^2\,\mathcal{P}\int_{\nu_{\rm thr}}^{+\infty} \mathrm{d}\nu'\; \frac{\mathrm{Im}_s A_i(\nu',t)}{\nu'\,(\nu'^2-\nu^2)}\,.\end{aligned} \tag{12}$$

These subtracted DR should converge for all 6 invariant amplitudes due to the two additional powers of ν' in the denominator, and they are essentially saturated by the πN intermediate states. In other words, the less known contributions of two and more pions as well as higher continua are small and may be treated reliably by simple models.

The price to pay for this alternative is the appearance of the subtraction functions $A_i(\nu = 0, t)$, which have to be determined at some small (negative) value of t. This was achieved by setting up once-subtracted DR, this time in the variable t [9] :

$$\begin{aligned}A_i(0,t) - A_i^{\rm B}(0,t) &= a_i \;+\; a_i^{t\text{-pole}} \\ &+\; \frac{t}{\pi}\left(\int_{(2m_\pi)^2}^{+\infty}\mathrm{d}t' - \int_{-\infty}^{-2m_\pi^2-4Mm_\pi}\mathrm{d}t'\right)\frac{\mathrm{Im}_t A_i(0,t')}{t'\,(t'-t)},\end{aligned} \tag{13}$$

where the six coefficients $a_i \equiv A_i(0,0) - A_i^{\rm B}(0,0)$ are simply related to the six polarizabilities $\alpha, \beta, \gamma_1, \gamma_2, \gamma_3, \gamma_4$ (see ref. [9] for details), and where $a_i^{t\text{-pole}}$ represents, in the case of A_2, the contribution of the π^0 pole in the t-channel.

To evaluate the dispersion integrals, the imaginary part of the Compton amplitude due to the s-channel cuts in eq. (12) is determined, through the unitarity relation, from the scattering amplitudes of photoproduction on the nucleon. Due to the energy denominator $1/\nu'(\nu'^2-\nu^2)$ in the subtracted dispersion integrals, the most important contribution is from the πN intermediate states, while mechanisms involving more pions or heavier mesons in the intermediate states are largely suppressed. In ref. [9], the πN contribution was then evaluated using the pion photoproduction multipole amplitudes of ref. [11] at photon energies below 500 MeV, and at the higher energies using the SAID multipoles (SP98K solution) [12] as input. The multipion channels (in particular the $\pi\pi$N channels) were approximated by the inelastic decay channels of the πN resonances. It was found, however, that in the subtracted DR formalism, the sensitivity to the multipion channels is very small and that subtracted DR are essentially saturated at $\nu \approx 0.4$ GeV.

The subtracted t-channel dispersion integral in eq. (13) from $4m_\pi^2$ to $+\infty$ is essentially saturated by the imaginary part of the t-channel amplitude $\gamma\gamma \rightarrow \mathrm{N\bar{N}}$ due to $\pi\pi$ intermediate states. The dependence of the subtraction functions on momentum transfer t can be calculated by including the experimental information on the t-channel process through $\pi\pi$ intermediate states as $\gamma\gamma \rightarrow \pi\pi \rightarrow \mathrm{N\bar{N}}$. In ref. [9], a unitarized amplitude for the $\gamma\gamma \rightarrow \pi\pi$ subprocess was constructed, and a good description of the available data was found. This information is then combined with the $\pi\pi \rightarrow \mathrm{N\bar{N}}$ amplitudes determined from dispersion theory by analytical continuation of πN scattering. In this way, one avoids the uncertainties in Compton scattering associated with the two-pion continuum in the t-channel, usually modeled through the exchange of a somewhat fictitious σ-meson. The second integral in eq. (13) extends from $-\infty$ to $-2\,(m_\pi^2 + 2Mm_\pi) \approx -0.56$ GeV^2. As we address Compton scattering for photon energies below about 500 MeV, the value of t stays sufficiently small so that the denominator in the integral provides a rather large suppression, resulting in a small contribution. The contribution along the negative t-cut is estimated in the calculations [20] by saturation with Δ intermediate states. Altogether the remaining uncertainties in the s- and t-channel subtracted integrals due to unknown high-energy contributions, are estimated to be less than 1%. As a consequence, this subtracted DR formalism provides a direct cross check between Compton scattering and one-pion photoproduction.

Although all 6 subtraction constants a_1 to a_6 of eq. (13) could be used as fit parameters in the present formalism, the fit was restricted to the parameters a_1 and a_2, or equivalently to $\alpha - \beta$ and γ_π in [9]. The subtraction constants a_4, a_5 and a_6 were calculated through an unsubtracted sum rule (eq. (9) for $\nu = t = 0$). The remaining subtraction constant a_3, related to $\alpha + \beta$ by $\alpha + \beta = -(a_3 + a_6)/(2\pi)$, was fixed through Baldin's sum rule [5], using the value $\alpha + \beta = 13.69 \times 10^{-4}$ fm^3 [7].

2.3 Results for RCS observables

Since the polarizabilities enter as subtraction constants, the subtracted dispersion relations can be used to extract the nucleon polarizabilities from RCS data with a minimum of model dependence. The present formalism can be applied up to photon energies of about 500 MeV.

Below pion production threshold, RCS data were usually analyzed to extract α and β. However, it was shown that the sensitivity to γ_π is not at all negligible, especially at the backward angles and the higher energies, so that both $\alpha - \beta$ and γ_π should be fitted simultaneously [9].

RCS above pion threshold can serve as a complement to determine the polarizabilities, in particular the spin polarizabilities, and can provide valuable cross checks between Compton scattering and pion photoproduction, provided one can minimize the model uncertainties in the dispersion formalism. The three types of dispersion integrals of eqs. (12) and (13) in the formalism outlined here are evaluated as described above. As a representative result obtained within the subtracted DR formalism, the RCS differential cross-sections above pion threshold are shown in fig. 1 at fixed $\alpha - \beta = 10$ (here and in the following in units of 10^{-4} fm^3), while γ_π is varied between -27 (here and in the following in units of 10^{-4} fm^4) and -37 (for more details, see refs. [9,20]). By comparing all available data above pion threshold, it was concluded [9] that there is no consistency between the pion photoproduction data from MAMI (entering through the dispersion integrals) and available Compton scattering data, in particular when comparing with the LEGS data, which were used in the extraction of eq. (8) for γ_π. Therefore, new data in the Δ region are called for, some of which have recently become available [21]. An analysis of those unpolarized data in a dispersion formalism favors also a much more negative value for γ_π than extracted in eq. (8). The fit performed by ref. [21] yields $\alpha - \beta = 9.1 \pm 1.7(\mathrm{stat} + \mathrm{syst}) \pm 1.2(\mathrm{mod})$, when using a value of $\gamma_\pi = -37.6$.

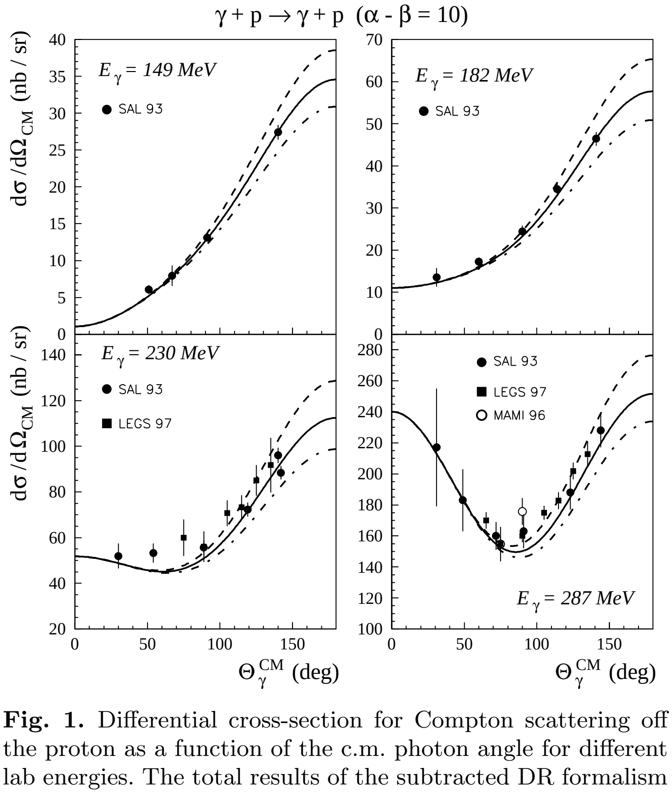

Fig. 1. Differential cross-section for Compton scattering off the proton as a function of the c.m. photon angle for different lab energies. The total results of the subtracted DR formalism are presented for fixed $\alpha - \beta = 10$ and different values of γ_π : $\gamma_\pi = -37$ (dashed-dotted lines), $\gamma_\pi = -32$ (full lines) and γ_π = -27 (dashed lines). The references to the data can be found in [9].

Besides the existing information from unpolarized data, a full study of the spin (or vector) polarizabilities will however require double polarization experiments. It was in fact shown [9] that the scattering of polarized photons on polarized protons is very sensitive to γ_π, in particular in the backward hemisphere and at energies between threshold and the Δ region. In addition, possible normalization problems can be avoided by measuring appropriate asymmetries. Therefore, future polarization experiments hold the promise to disentangle the scalar and vector polarizabilities of the nucleon with the help of the described subtracted DR formalism, and to further quantify the nucleon spin response in an external electromagnetic field.

2.4 Higher-order polarizabilities of the proton

As outlined above, the electric and magnetic polarizabilities arise as $O(\nu^2)$ corrections to the lowest-order (Thomson) scattering amplitude. One can then ask the question whether Compton scattering can also provide additional proton structure information via the use of higher-order polarizabilities. If one extends the analysis to consider spin-averaged $O(\nu^4)$ terms (see ref. [22] for details), four new structures fulfill the requirements of gauge, P, and T invariance. Two new quantities, $\alpha^{\mathrm{p}}_{E\nu}$ and $\beta^{\mathrm{p}}_{M\nu}$, represent dispersive corrections to the lowest-order static polarizabilities, α and β respectively, and describe the response of the system to time-dependent fields. Two more quantities α^{p}_{E2}, β^{p}_{M2}, represent quadrupole polarizabilities and measure the electric and magnetic quadrupole moments induced in a system by the presence of an applied field gradient.

As to the experimental evaluation of such structure probes, it is, of course, in principle possible to extract them directly from Compton cross-section measurements. However, it is already clear from the previous discussion of present data, that isolating such pieces from other terms which affect the cross-section at energies above ~ 100 MeV is virtually impossible since additional higher-order effects soon become equally important. Thus an alternative procedure is required, which is made possible by the validity of dispersion relations. Within the subtracted DR formalism of ref. [9] outlined above, those *higher order* terms in the expansion of the Compton amplitudes A_i can be reasonably evaluated as in [22]. These higher-order polarizabilities can be expressed in terms of appropriate derivatives of the RCS invariant amplitudes A_i at $t, \nu^2 = 0$, denoted by $a_{i,t}, a_{i,\nu}$. In terms of subtracted DR's, they take the form

$$a_{i,\nu} = \frac{2}{\pi} \int_{\nu_{\mathrm{thr}}}^{\infty} \mathrm{d}\nu' \frac{\mathrm{Im}_s A_i(\nu', t=0)}{\nu'^3}, \tag{14}$$

$$a_{i,t} = \frac{1}{\pi} \left(\int_{4m_\pi^2}^{\infty} - \int_{-\infty}^{-4Mm_\pi - 2m_\pi^2} \mathrm{d}t' \frac{\mathrm{Im}_t A_i(0,t')}{t'^2} \right). \tag{15}$$

The higher-order polarizabilities are then obtained as linear combinations of the $a_{i,t}$ and $a_{i,\nu}$ (for details see [22]). The subtracted DR in eqs. (14, 15) were evaluated as described above and yield (all in units of 10^{-4} fm^5) :

$$\begin{aligned} \alpha^{\mathrm{p}}_{E\nu} &= -3.84 - 0.19 + 0.06, \\ \beta^{\mathrm{p}}_{M\nu} &= +9.29 + 0.15 - 0.07, \\ \alpha^{\mathrm{p}}_{E2} &= +29.31 - 0.10 - 0.17, \\ \beta^{\mathrm{p}}_{M2} &= -24.33 + 0.10 - 0.34\,, \end{aligned} \tag{16}$$

where the second and third entries on the rhs of eq. (16) estimate the uncertainties in the s- and t-channel dispersion integrals.

The values of eq. (16) were then confronted in [22] with the predictions of HBChPT at $\mathcal{O}(p^3)$

$$\begin{aligned} \mathcal{O}(p^3): \quad & \alpha^{\mathrm{p}}_{E\nu} = 2.4, \quad \beta^{\mathrm{p}}_{M\nu} = 3.7, \\ & \alpha^{\mathrm{p}}_{E2} = 22.1, \quad \beta^{\mathrm{p}}_{M2} = -9.5\,. \end{aligned} \tag{17}$$

By comparing eq. (16) and (17) one finds that the size of α^{p}_{E2} is about right, while for both β^{p}_{M2} and $\beta^{\mathrm{p}}_{M\nu}$ the sign and order of magnitude is correct but additional contributions are called for. The most serious problem lies in the experimental determination of $\alpha_{E\nu}$ which is negative in contradistinction to the chiral prediction and to sum rule arguments which assert its positivity. To see if inclusion of $\Delta(1232)$ degrees of freedom can help to resolve the above discrepancies, these quantities were also calculated in [22] in HBChPT to $O(\epsilon^3)$, with the result :

$$\begin{aligned} \mathcal{O}(\epsilon^3): \quad & \alpha^{\mathrm{p}}_{E\nu} = 1.7, \quad \beta^{\mathrm{p}}_{M\nu} = 7.5, \\ & \alpha^{\mathrm{p}}_{E2} = 26.2, \quad \beta^{\mathrm{p}}_{M2} = -12.3\,. \end{aligned} \tag{18}$$

Except for the sign problem with $\alpha^{\mathrm{p}}_{E\nu}$ indicated above, which persists in the ϵ-expansion, the changes are generally helpful, although the magnetic quadrupole polarizability is still somewhat underpredicted.

In [22], the described analysis was also extended to higher-order contributions $O(\nu^5)$ to the proton spin polarizabilities, for which 8 new structures were found. A dispersive evaluation of those higher-order spin polarizabilities showed a qualitative agreement with HBChPT $O(\epsilon^3)$ predictions.

Recently, an evaluation of the higher-order polarizabilities of the proton in HBChPT to $O(p^4)$ has been reported [23], providing an important new testing ground for the chiral predictions. It was found [23] that the $O(p^4)$ HBChPT result for the 4 quadrupole polarizabilities and the 8 spin polarizabilities at $O(\nu^5)$ of the proton are in encouraging good agreement with the DR estimates of ref. [22].

In summary, the subtracted DR formalism presented not only provides a formalism to extract the lowest-order nucleon polarizabilities from present and forthcoming RCS data with a minimum of model dependence. It can also be used to obtain information about higher-order polarizabilities of the proton, in this way providing a great deal of additional nucleon structure information.

3 Virtual Compton scattering (VCS) and generalized nucleon polarizabilities

3.1 Introduction

The nucleon structure information obtained through RCS, as discussed in section 2, can be generalized by virtual Compton scattering (VCS) below pion threshold. VCS can be interpreted as electron scattering off a target polarized by the presence of constant electric and magnetic fields. To see how VCS generalizes the RCS process, it is useful to think of the analogy with the electromagnetic form factors. Their measurement through elastic electron-nucleon scattering reveals the spatial distribution of the charge and magnetization distributions of the target, whereas a real photon is only sensitive to the overall charge and magnetization of the target. The physics addressed with VCS is then the same as if one were performing an elastic electron scattering experiment on a target placed between the plates of a capacitor or between the poles of a magnet. In this way one studies the spatial distributions of the polarization densities of the target, by means of the generalized polarizabilities, which are functions of the square of the four-momentum, Q^2, transferred by the electron.

Experimentally, the VCS process is accessed through the electroproduction of photons, and we consider in all of the following the reaction on a proton target, *i.e.* the reaction ep → epγ. One immediately sees a difference with regard to the RCS γp → γp reaction, because in the ep → epγ reaction, the final photon can be emitted either by the proton, giving access to the VCS process, or by the electrons, which is referred to as the Bethe-Heitler (BH) process. The BH amplitude can be calculated exactly in QED, provided one knows the elastic form factors of the proton. Therefore it contains no new information on the structure. Unfortunately, light particles such as electrons radiate much more than the heavy proton. Therefore the BH process generally dominates or at least interferes strongly with the VCS process, and this may complicate the interpretation of the ep → epγ reaction. The only way out of this problem is either to find kinematical regions where the BH process is suppressed or to have a very good theoretical control over the interference between the BH and the VCS amplitudes, as will be discussed below.

Assuming that this problem is fixed, one can then proceed to extract the nucleon structure information from VCS. In doing so, care has to be taken to separate the trivial response of the target, due to its global charge and/or a global magnetic moment. Indeed, if we put a proton in an electric field, the first effect we observe is that it moves as a whole. Similarly, the magnetic field produces a precession of the magnetic moment. This problem is absent when one studies the polarizability of a macroscopic sample because it can be fixed in space by appropriate means, which is not possible for the proton. This absence of a restoring force explains why the trivial response due to the motion of charge and magnetic moment dominates over the response of the internal degrees of freedom. This is the physical origin of the low-energy theorem (LET) [24] for VCS. All what is needed to calculate this part of the response, are the parameters which control the motion, that is the mass, the charge, and the magnetic moment. Once the motion is known, one can compute the amplitude for scattering an electron on this moving proton, the so-called Born amplitude. Having separated the trivial response, one can parametrize the structure part of interest in the VCS process through the so-called generalized polarizabilities (GP's) as in ref. [25].

3.2 Definition of generalized polarizabilities

The known BH + Born parts of the VCS amplitude at low energy start at order $1/\mathrm{q}'$ in an expansion in the outgoing photon energy q'. The LET [24] asserts that the non trivial part of the VCS amplitude, the so-called non-Born part (denoted by H_{NB}), begins at order q'. There is of course also a contribution of order q' in the BH + Born amplitude, but this term is exactly known and therefore can be subtracted, at least in principle. So what is needed next is an adequate parametrization of H_{NB}. For this purpose, a multipole expansion (in the c.m. frame) was performed in [25] in order to take advantage of angular momentum and parity conservation. The behaviour of the non-Born VCS amplitude H_{NB} at low energy ($\mathrm{q}' \to 0$) but at arbitrary three-momentum q of the virtual photon, was then parametrized by 10 functions of q defined by

$$\text{Limit of } \frac{1}{\mathrm{q}'}\frac{1}{\mathrm{q}^L} H_{\mathrm{NB}}^{(\rho' 1, \rho L)S}(\mathrm{q}', \mathrm{q}) \text{ when } \mathrm{q}' \to 0. \qquad (19)$$

In this notation, ρ (ρ') refers to the electric (2), magnetic (1) or longitudinal (0) nature of the initial (final) photon, L ($L' = 1$) represents the angular momentum of the initial (final) photon, whereas S differentiates between the spin-flip ($S = 1$) and non spin-flip ($S = 0$) character of the electromagnetic transition at the nucleon side. As the angular momentum of the outgoing photon is L' = 1, this leads to 10 q-dependent GP's, denoted generically by $P^{(\rho' L', \rho L)S}(\mathrm{q})$. By imposing the constraints due to nucleon crossing combined with charge conjugation invariance on the VCS amplitude, it was shown however in [26,27] that 4 of the GP's can be eliminated. Thus only 6 GP's , *e.g.*, [1]

$$\begin{aligned}
&P^{(01,01)0}(\mathrm{q}), P^{(11,11)0}(\mathrm{q}),\\
&P^{(01,01)1}(\mathrm{q}), P^{(11,11)1}(\mathrm{q}), P^{(11,02)1}(\mathrm{q}), P^{(01,12)1}(\mathrm{q}), \qquad (20)
\end{aligned}$$

are necessary to give the low-energy behaviour of H_{NB}.

In the limit q → 0 for the GP's, one finds the following relations with the polarizabilities (in gaussian units) of RCS, as discussed in section 2 [28] :

$$\begin{aligned}
P^{(01,01)0}(0) &= -\frac{1}{\alpha_{\mathrm{em}}}\sqrt{\frac{2}{3}}\,\alpha\ ,\\
P^{(11,11)0}(0) &= -\frac{1}{\alpha_{\mathrm{em}}}\sqrt{\frac{8}{3}}\,\beta\ ,\\
P^{(01,12)1}(0) &= -\frac{1}{\alpha_{\mathrm{em}}}\frac{\sqrt{2}}{3}\,\gamma_3\ ,
\end{aligned}$$

$$
\begin{aligned}
&P^{(11,02)1}(0) = -\frac{1}{\alpha_{\rm em}}\,\frac{2\sqrt{2}}{3\sqrt{3}}\,(\gamma_2+\gamma_4)\ ,\\
&P^{(01,01)1}(0) = 0\ ,\\
&P^{(11,11)1}(0) = 0\ ,
\end{aligned}
\tag{21}
$$

where $\alpha_{\rm em} = 1/137.036$ is the QED fine structure constant.

3.3 VCS observables

We next discuss how one can analyze ep → epγ observables to extract the 6 GP's of eq. (20).

The VCS unpolarized squared amplitude is denoted by $\mathcal{M}$. Besides, one can consider VCS double polarization observables, which are denoted by $\Delta\mathcal{M}(h,i)$ for an electron of helicity h, and which are defined as a difference of the squared amplitudes for recoil (or target) proton spin orientation in the direction and opposite to the axis i $(i = x, y, z)$ (see ref. [29] for details). In an expansion in q$'$, $\mathcal{M}$ and $\Delta\mathcal{M}$ take the form

$$
\begin{aligned}
\mathcal{M}^{\rm exp} &= \frac{\mathcal{M}^{\rm exp}_{-2}}{{\rm q}'^2} + \frac{\mathcal{M}^{\rm exp}_{-1}}{{\rm q}'} + \mathcal{M}^{\rm exp}_0 + O({\rm q}'),\\
\Delta\mathcal{M}^{\rm exp} &= \frac{\Delta\mathcal{M}^{\rm exp}_{-2}}{{\rm q}'^2} + \frac{\Delta\mathcal{M}^{\rm exp}_{-1}}{{\rm q}'} + \Delta\mathcal{M}^{\rm exp}_0 + O({\rm q}')\,.
\end{aligned}
\tag{22}
$$

Due to the LET, the threshold coefficients $\mathcal{M}_{-2}$, $\mathcal{M}_{-1}$, $\Delta\mathcal{M}_{-2}$, $\Delta\mathcal{M}_{-1}$ are known. The information on the GP's is contained in $\mathcal{M}^{\rm exp}_0$ and $\Delta\mathcal{M}^{\rm exp}_0$. These coefficients contain a part which comes from the (BH+Born) amplitude and another one which is a linear combination of the GP's with coefficients determined by the kinematics.

The unpolarized observable $\mathcal{M}^{\rm exp}_0$ was obtained by ref. [25] in terms of 3 structure functions $P_{LL}({\rm q})$, $P_{TT}({\rm q})$, $P_{LT}({\rm q})$, which are linear combinations of the 6 GP's,

$$
\begin{aligned}
\mathcal{M}^{\rm exp}_0 - \mathcal{M}^{\rm BH+Born}_0 &= 2K_2\left\{v_1\left[\epsilon P_{LL}({\rm q}) - P_{TT}({\rm q})\right]\right.\\
&\left. + \left(v_2 - \frac{\tilde{q}_0}{\rm q}v_3\right)\sqrt{2\varepsilon\,(1+\varepsilon)}P_{LT}({\rm q})\right\},
\end{aligned}
\tag{23}
$$

where $K_2, \epsilon, \tilde{q}_0, v_1, v_2, v_3$ are kinematical quantities (for details see ref. [1]).

The three double-polarization observables $\Delta\mathcal{M}^{\rm exp}_0(h,i)$ $(i = x, y, z)$ were expressed by [29] in terms of three new independent structure functions $P^z_{LT}({\rm q})$, $P'^z_{LT}({\rm q})$, and $P'^{\perp}_{LT}({\rm q})$, which are also linear combinations of the 6 GP's,

$$
\begin{aligned}
&\Delta\mathcal{M}^{\rm exp}_0(h,z) - \Delta\mathcal{M}^{\rm BH+Born}_0(h,z)\\
&= 4(2h)K_2\left\{-v_1\sqrt{1-\varepsilon^2}P_{TT}({\rm q}) + v_2\sqrt{2\varepsilon\,(1-\varepsilon)}P^z_{LT}({\rm q})\right.\\
&\quad\left. + v_3\sqrt{2\varepsilon\,(1-\varepsilon)}P'^z_{LT}({\rm q})\right\},\\
&\Delta\mathcal{M}^{\rm exp}_0(h,x) - \Delta\mathcal{M}^{\rm BH+Born}_0(h,x)\\
&= 4(2h)K_2\left\{v^x_1\sqrt{2\varepsilon\,(1-\varepsilon)}\,P^{\perp}_{LT}({\rm q}) + v^x_2\sqrt{1-\varepsilon^2}\,P^{\perp}_{TT}({\rm q})\right.\\
&\quad\left. + v^x_3\sqrt{1-\varepsilon^2}\,P'^{\perp}_{TT}({\rm q}) + v^x_4\sqrt{2\varepsilon\,(1-\varepsilon)}\,P'^{\perp}_{LT}({\rm q})\right\},\\
&\Delta\mathcal{M}^{\rm exp}_0(h,y) - \Delta\mathcal{M}^{\rm BH+Born}_0(h,y)\\
&= 4(2h)K_2\left\{v^y_1\sqrt{2\varepsilon\,(1-\varepsilon)}\,P^{\perp}_{LT}({\rm q}) + v^y_2\sqrt{1-\varepsilon^2}\,P^{\perp}_{TT}({\rm q})\right.\\
&\quad\left. + v^y_3\sqrt{1-\varepsilon^2}\,P'^{\perp}_{TT}({\rm q}) + v^y_4\sqrt{2\varepsilon\,(1-\varepsilon)}\,P'^{\perp}_{LT}({\rm q})\right\},
\end{aligned}
\tag{24}
$$

where $v^x_1, ..., v^x_4, v^y_1, ..., v^y_4$ are kinematical coefficients. The other structure functions in eq. (24) can be expressed in terms of $P_{LL}, P_{TT}, P_{LT}, P^z_{LT}, P'^z_{LT}, P'^{\perp}_{LT}$ [1]. Therefore, measuring those 6 structure functions amounts to determine the 6 independent GP's.

3.4 Results for VCS observables below pion threshold

In the previous sections, the observables of the ep → epγ reaction below pion threshold were outlined, and it was shown how the nucleon structure effect can be parametrized in terms of 6 independent GP's.

To access the GP's, the experimental strategy of VCS in the threshold region consists of two steps. First, one measures the VCS cross-section at several values of the outgoing photon energy. At low energies, the measurement of the VCS observables provides a test of the LET. Once the LET is verified, the relative effect of the GP's can be extracted using eqs. (23,24).

The predictions for the Bethe-Heitler (BH) and Born cross-sections below pion threshold are shown in fig. 2. The BH cross-section has a characteristic angular shape and displays two "spikes", which occur when the direction of the outgoing photon coincides with either the initial or final electron directions. In these regions, the cross-section is completely dominated by the BH contributions. In order to determine the VCS contribution, one clearly has to

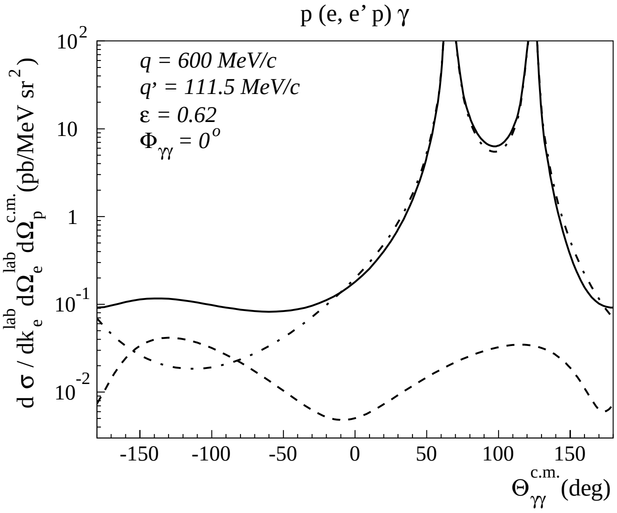

Fig. 2. Results for the BH (dashed-dotted curve), Born (dashed curve) and BH+Born (full curve) p(e, e$'$ p)γ differential cross-sections in MAMI kinematics : q = 600 MeV/c, q$'$ = 111.5 MeV/c and $\epsilon = 0.62$, as function of the c.m. angle $\Theta^{\gamma\gamma}_{\rm c.m.}$ between real and virtual photon, and for in-plane kinematics. Calculations from ref. [30].

minimize the BH contamination by detecting the photon in the half-plane opposite to the electron directions.

The first dedicated VCS experiment has been performed at MAMI, and for the first time two combinations (see eq. (23)) of GP's have been determined at $Q^2 = 0.33$ GeV^2 and photon polarization $\epsilon = 0.62$ [31],

$$P_{LL}(Q^2) - \frac{1}{\epsilon} P_{TT}(Q^2) = (23.7 \pm 2.2 \pm 0.6 \pm 4.3)\ \mathrm{GeV}^2 ,$$
$$P_{LT}(Q^2) = (-5.0 \pm 0.8 \pm 1.1 \pm 1.4)\ \mathrm{GeV}^2. \qquad (25)$$

VCS experiments at higher Q^2 (1 - 2 GeV^2) at JLab [32], and at lower Q^2 at MIT-Bates [33] have already been performed, and are under analysis at this time.

The GP's have been calculated in various approaches and nucleon structure models, ranging from constituent quark models [25,34], a relativistic effective Lagrangian model [30], and the linear σ-model [35] to ChPT [36,37]. The GP's teach us about the interplay between nucleon-core excitations and pion-cloud effects, which are described differently in the various models. We focus here on the calculation of the GP's in HBChPT to $\mathcal{O}(p^3)$, as it takes account of Nπ-loop contributions in a systematic way. The $\mathcal{O}(p^3)$ calculation yields for the two measured combinations at $Q^2 = 0.33$ GeV^2 and $\epsilon = 0.62$ of eq. (25) the values [37] :

$$\begin{aligned} \mathcal{O}(p^3): \quad P_{LL} - P_{TT}/\epsilon &= 26.3\ \ \mathrm{GeV}^2, \\ P_{LT} &= -5.7\ \ \mathrm{GeV}^2, \end{aligned} \qquad (26)$$

which are in astonishing agreement with the experimentally determined values of eq. (25). In particular, the $\mathcal{O}(p^3)$ ChPT calculation predicts quite large values for the spin GP's. As for the case of the RCS polarizabilities, the importance of the $\mathcal{O}(p^4)$ corrections remains to be checked.

If one wants to extract the different polarizabilities from experiment, and in particular in case of the spin polarizabilities, an unpolarized experiment is not sufficient as it gives access to 3 independent response functions only. To further separate the polarizabilities, one has to resort to double-polarization observables. Experimentally, at the existing high-duty-cycle electron facilities with polarized electron beams such as MAMI, MIT-Bates and JLab, double polarization VCS experiments can be performed by measuring the recoil polarization of the outgoing nucleon with a focal plane polarimeter. An experiment at MAMI has already been proposed [38].

In fig. 3, the double-polarization asymmetry of eq. (24), with proton recoil polarization either along the x- or z- directions, is shown at q = 600 MeV/c for in-plane kinematics. It is seen that the asymmetry yields a very large value (between 0.6 and 0.7) if the final proton is polarized parallel to the virtual photon.

3.5 Dispersion relation formalism for VCS

At present, VCS experiments at low outgoing photon energies are analyzed in terms of low-energy expansions (LEXs) of eq. (22). In the LEX, the non-Born response of the system to the quasi-constant electromagnetic field of the low energetic photon is proportional to the GP's, as expressed in eqs. (23,24). As the sensitivity of the VCS cross-sections to the GP's grows with the photon energy, it is advantageous to go to higher photon energies, provided one can keep the theoretical uncertainties under control when crossing the pion threshold. The situation can be compared to RCS, for which one uses a dispersion relation formalism as discussed in section 2, to extract the polarizabilities at energies above pion threshold, with generally larger effects on the observables.

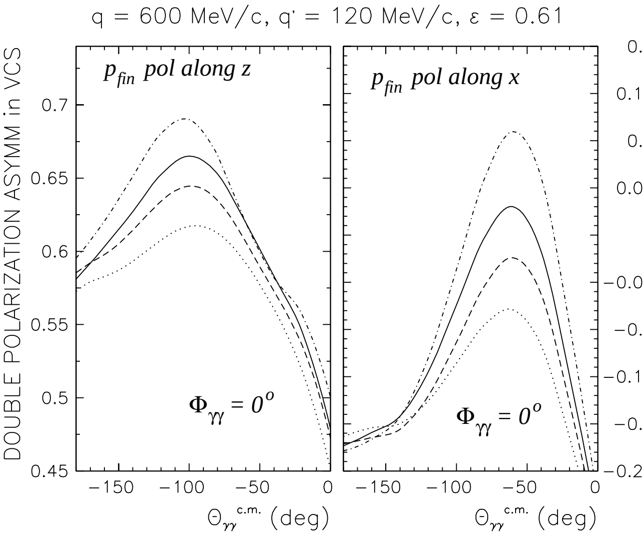

Fig. 3. VCS double-polarization asymmetries (polarized electron, proton recoil polarization along either the x- or z-directions) in MAMI kinematics ($Q^2 = 0.33$ GeV^2) as function of the c.m. angle between real and virtual photon. The BH + Born result is shown by the dashed curves. The other curves show predictions from different model contributions calculated in ref. [29], to which we refer for details.

In order to go to higher energies and to check the validity of LEXs at these higher energies, a dispersion relation analysis for VCS has been developed very recently [39, 40], which will allow to extract the GP's from data over a larger energy range. The same formalism also provides for the first time a dispersive evaluation of 4 GP's.

To set up a dispersion formalism for the VCS process, one starts from the helicity amplitudes :

$$T_{\lambda' s'; \lambda s} \;=\; -\,e^2 \varepsilon_\mu(q,\lambda)\, \varepsilon_\nu^{'*}(q',\lambda')\, \bar{u}(p',s') \mathcal{M}^{\mu\nu} u(p,s), \qquad (27)$$

with e the electric charge, q (q') the four-vectors of the virtual (real) photon in the VCS process, and p (p') the four-momenta of the initial (final) nucleons respectively. The nucleon helicities are denoted by $s, s' = \pm 1/2$, and $u, \bar{u}$ are the nucleon spinors. The initial virtual photon has helicity $\lambda = 0, \pm 1$ and polarization vector ε_μ, whereas the final real photon has helicity $\lambda' = \pm 1$ and polarization vector $\varepsilon_\nu^{'}$. The VCS process is characterized by 12 independent helicity amplitudes $T_{\lambda' s'; \lambda s}$.

The VCS tensor $\mathcal{M}^{\mu\nu}$ in eq. (27) is then expanded into a basis of 12 independent gauge invariant tensors $\rho_i^{\mu\nu}$,

$$\mathcal{M}^{\mu\nu} \;=\; \sum_{i=1}^{12} F_i(Q^2, \nu, t)\, \rho_i^{\mu\nu} \;, \tag{28}$$

as introduced in ref. [26] (starting from the amplitudes of ref. [41]). The amplitudes F_i in eq. (28) contain all nucleon structure information and are functions of 3 invariants for the VCS process : $Q^2 \equiv -q^2$, $\nu = (s-u)/(4m_\mathrm{N})$ which is odd under $s \leftrightarrow u$ crossing, and t. The Mandelstam invariants s, t and u for VCS are defined by $s = (q+p)^2$, $t = (q-q')^2$, and $u = (q-p')^2$, with the constraint $s + t + u = 2m_\mathrm{N}^2 - Q^2$, and m_N is the nucleon mass.

Nucleon crossing combined with charge conjugation provides the following constraints on the amplitudes F_i [1] at arbitrary virtuality Q^2 :

$$F_i\left(Q^2, -\nu, t\right) = F_i\left(Q^2, \nu, t\right) \qquad (i = 1, ..., 12). \tag{29}$$

With the choice of the tensor basis of ref. [26], the resulting non-Born amplitudes F_i^NB (i = 1,...,12) are free of all kinematical singularities and constraints.

Assuming further analyticity and an appropriate high-energy behavior, the non-Born amplitudes $F_i^\mathrm{NB}(Q^2, \nu, t)$ fulfill unsubtracted dispersion relations (DR's) with respect to the variable ν at fixed t and fixed virtuality Q^2 :

$$\mathrm{Re}\, F_i^\mathrm{NB}(Q^2, \nu, t) = \frac{2}{\pi}\mathcal{P}\int_{\nu_\mathrm{thr}}^{+\infty} \mathrm{d}\nu' \frac{\nu'\, \mathrm{Im}_s F_i(Q^2, \nu', t)}{\nu'^2 - \nu^2}, \tag{30}$$

with $\mathrm{Im}_s F_i$ the discontinuities across the s-channel cuts of the VCS process. Since pion production is the first inelastic channel, $\nu_\mathrm{thr} = m_\pi + (m_\pi^2 + t/2 + Q^2/2)/(2m_\mathrm{N})$, where m_π denotes the pion mass.

The unsubtracted DR's of eq. (30) require that at sufficiently high energies ($\nu \to \infty$ at fixed t and fixed Q^2) the amplitudes $\mathrm{Im}_s F_i(Q^2, \nu, t)$ (i = 1,...,12) drop fast enough such that the integrals are convergent and the contributions from the semi-circle at infinity can be neglected. It turns out that for two amplitudes, F_1 and F_5, an unsubtracted dispersion integral as in eq. (30) does not exist [39], whereas the other 10 amplitudes can be evaluated through unsubtracted dispersion integrals. This situation is similar as for RCS, where 2 of the 6 invariant amplitudes cannot be evaluated by unsubtracted dispersion relations either [2].

The unsubtracted DR formalism for VCS also allows to predict 4 of the 6 GP's. The appropriate limit in the definition of the GP's is $\mathrm{q}' \to 0$ at finite q (see eq. (19)), which corresponds in terms of VCS invariants to $\nu \to 0$ and $t \to -Q^2$ at finite Q^2. One can therefore express the GP's in terms of the VCS amplitudes F_i at the point $\nu = 0$, $t = -Q^2$ at finite Q^2, denoted in the following as : $\bar{F}_i(Q^2) \;\equiv\; F_i^\mathrm{NB}\left(Q^2, \nu = 0, t = -Q^2\right)$. The relations between the GP's and the $\bar{F}_i(Q^2)$ can be found in ref. [26]. From the high-energy behavior for the VCS invariant amplitudes, it follows that one can evaluate the $\bar{F}_i$ (for $i \neq$ 1, 5) through the unsubtracted DR's

$$\bar{F}_i(Q^2) \;=\; \frac{2}{\pi}\int_{\nu_\mathrm{thr}}^{+\infty} \mathrm{d}\nu' \; \frac{\mathrm{Im}_s F_i(Q^2, \nu', t = -Q^2)}{\nu'} \;. \tag{31}$$

Unsubtracted DR's for the GP's will therefore hold for those combinations of GP's that do not depend upon the amplitudes $\bar{F}_1$ and $\bar{F}_5$ [2]. Among the 6 GP's, the following 4 combinations of GP's were found in ref. [39] :

$$P^{(01,01)0} + \frac{1}{2}P^{(11,11)0} = \frac{-2}{\sqrt{3}}\left(\frac{E + m_\mathrm{N}}{E}\right)^{1/2} m_\mathrm{N}\, \tilde{q}_0 \times \left\{\frac{\mathrm{q}^2}{\tilde{q}_0^2}\,\bar{F}_2 + \left(2\,\bar{F}_6 + \bar{F}_9\right) - \bar{F}_{12}\right\}, \tag{32}$$

$$P^{(01,01)1} = \frac{1}{3\sqrt{2}}\left(\frac{E + m_\mathrm{N}}{E}\right)^{1/2} \tilde{q}_0 \times \left\{\left(\bar{F}_5 + \bar{F}_7 + 4\,\bar{F}_{11}\right) + 4\,m_\mathrm{N}\,\bar{F}_{12}\right\}, \tag{33}$$

$$P^{(01,12)1} - \frac{1}{\sqrt{2}\,\tilde{q}_0}P^{(11,11)1} = \frac{1}{3}\left(\frac{E + m_\mathrm{N}}{E}\right)^{1/2} \frac{m_\mathrm{N}\,\tilde{q}_0}{\mathrm{q}^2} \times \left\{\left(\bar{F}_5 + \bar{F}_7 + 4\,\bar{F}_{11}\right) + 4\,m_\mathrm{N}\left(2\,\bar{F}_6 + \bar{F}_9\right)\right\}, \tag{34}$$

$$P^{(01,12)1} + \frac{\sqrt{3}}{2}P^{(11,02)1} = \frac{1}{6}\left(\frac{E + m_\mathrm{N}}{E}\right)^{1/2} \frac{\tilde{q}_0}{\mathrm{q}^2} \times \left\{\tilde{q}_0\left(\bar{F}_5 + \bar{F}_7 + 4\,\bar{F}_{11}\right) + 8\,m_\mathrm{N}^2\left(2\,\bar{F}_6 + \bar{F}_9\right)\right\}, \tag{35}$$

where $E = \sqrt{\mathrm{q}^2 + m_\mathrm{N}^2}$ denotes the initial proton c.m. energy, and $\tilde{q}_0 = m_\mathrm{N} - E$ the virtual photon c.m. energy in the limit $\mathrm{q}' = 0$. Unfortunately, the 4 combinations of GP's of eqs. (32)-(35) can at present not yet be compared with the data. In particular, the only unpolarized experiment [31] measured two structure functions which cannot be evaluated in an unsubtracted DR formalism, as they contain in addition to $P^{(01,01)0} + 1/2P^{(11,11)0}$ of eq. (32), which is proportional to $\alpha + \beta$ at $Q^2 = 0$, also the generalization of $\alpha - \beta$.

The 4 combinations of GP's on the lhs of eqs. (32)-(35) can then be evaluated by unsubtracted DR's, from the dispersion integrals of eq. (31) for the $\bar{F}_i(Q^2)$. To this end, the imaginary parts $\mathrm{Im}_s F_i$ in eq. (31) have to be calculated by use of unitarity. For the VCS helicity amplitudes of eq. (27) (denoted for short by T_{fi}), the unitarity equation reads

$$2\,\mathrm{Im}_s\, T_{fi} = \sum_X (2\pi)^4 \delta^4(P_X - P_i) T_{Xf}^\dagger\, T_{Xi} \;, \tag{36}$$

where the sum runs over all possible intermediate states X that can be formed. In ref. [39], the dispersion integrals of eq. (31) were saturated by the dominant contribution of the πN intermediate states. For the pion photo- and

---

[1] In [39], 4 of the 12 amplitudes of [26] were redefined by dividing them through ν, such that all of them are even functions of ν. This simplifies the formalism since only one type of dispersion integrals needs to be considered then.

[2] $\bar{F}_5$ can appear however in the combination $\bar{F}_5 + 4\,\bar{F}_{11}$, in which the π^0-pole drops out, and which has a high-energy behavior leading to a convergent integral (see ref. [39]).

electroproduction helicity amplitudes in the range $Q^2 \leq 0.5$ GeV^2, the phenomenological analysis of MAID [42] was used, which contains both resonant and non-resonant pion production mechanisms.

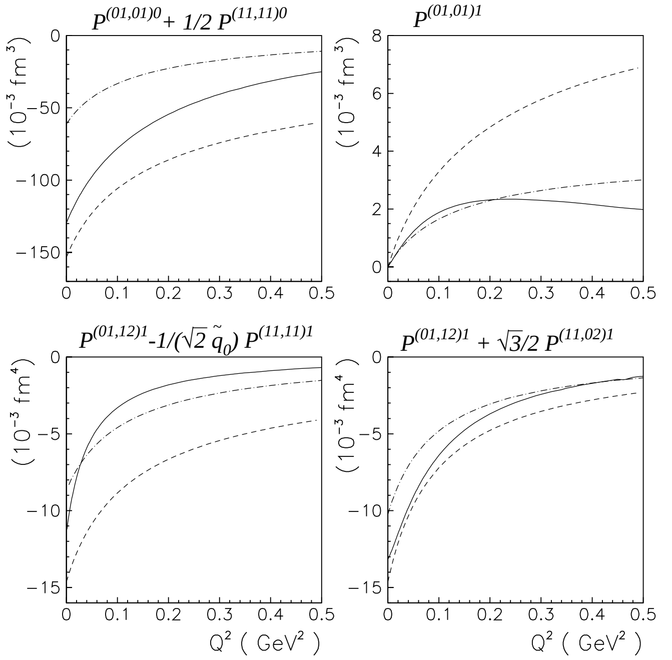

Fig. 4. Dispersion results [39] for 4 of the generalized polarizabilities of the proton (full curves), compared with results of $O(p^3)$ HBChPT [36,37] (dashed curves) and the linear σ-model [35] (dash-dotted curves).

In fig. 4, the results for the 4 combinations of GP's of eqs. (32)-(35) are shown in the DR formalism, and compared to the results of the $O(p^3)$ heavy-baryon chiral perturbation theory (HBChPT) [36,37] and the linear σ-model [35]. The πN contribution to the sum $P^{(01,01)0} + 1/2P^{(11,11)0}$ gives only about 80% of the Baldin sum rule [7], because of a non-negligible high-energy contribution (of heavier intermediate states) to the photoabsorption cross-section entering the sum rule, which is not estimated here. On the other hand, for the 3 combinations of spin polarizabilities of eqs. (33)-(35), the dispersive estimates with πN states are expected to provide a rather reliable guidance. By comparing the DR results with those of HBChPT at $O(p^3)$, one remarks a rather good agreement for $P^{(01,12)1} + \sqrt{3}/2P^{(11,02)1}$, whereas for the GP's $P^{(01,01)1}$ and $P^{(01,12)1}$ - $1/(\sqrt{2}\,\tilde{q}_0)P^{(11,11)1}$, the dispersive results drop much faster with Q^2. This trend is also seen in the relativistic linear σ-model, which takes account of some higher orders in the chiral expansion. It remains to be checked how the $\mathcal{O}(p^4)$ corrections in HBChPT change this comparison with the DR estimates.

To complete the DR formalism for VCS, one further needs to construct the VCS amplitudes F_1 and F_5, for which the unsubtracted dispersion integrals of eq. (30) do not converge. One strategy is to proceed in an analogous way as has been proposed in ref. [2] in the case of RCS. The unsubtracted dispersion integrals for F_1 and F_5 are evaluated along the real ν-axis in a finite range $-\nu_{\max} \leq \nu \leq +\nu_{\max}$ (with $\nu_{\max} \approx 1.5$ GeV). The integral along a semi-circle of finite radius $\nu_{\max}$ in the complex ν-plane is described by the asymptotic contribution F_i^{as}, which is parametrized by t-channel poles (*e.g.*, for $Q^2 = 0$, F_1^{as} corresponds to σ-exchange, and F_5^{as} to π^0-exchange).

A full study of VCS observables within such a dispersion formalism, including a parametrization of the two asymptotic contributions, is presently underway [43]. This will yield a formalism to extract the nucleon GP's over a larger range of energies from both unpolarized and polarized VCS data.

4 Compton scattering at large momentum transfer and the nucleon distribution amplitude

4.1 Introduction

Besides the low-energy region, as discussed in section 2, RCS will also provide access to information on the partonic structure of the nucleon at sufficiently large momentum transfer.

This regime is defined by requiring that all three Mandelstam variables (s, t, u) be large with respect to a typical hadronic scale, say 1 GeV. In this case there is a prejudice (actually proven in the case of elastic electron scattering [44]) that the amplitude factorizes in a soft non-perturbative part, the distribution amplitude, and a hard scattering kernel which is calculable from perturbative QCD (PQCD). Because of asymptotic freedom, the perturbative approach must be to some degree relevant to the hard-scattering regime. However, since the binding of the quarks and gluons in the hadrons is a long distance, non-perturbative effect, the description of the reaction requires a consistent analysis of both large and small scales. When the reaction is hard enough, the relative velocities of the participating particles are nearly lightlike. Time dilatation increases the lifetime of the quantum configurations which build the hadron. As a result, the partonic content, as seen by the other particles, is frozen. Moreover, due to the apparent contraction of the hadron size, the time during which momentum can be exchanged is

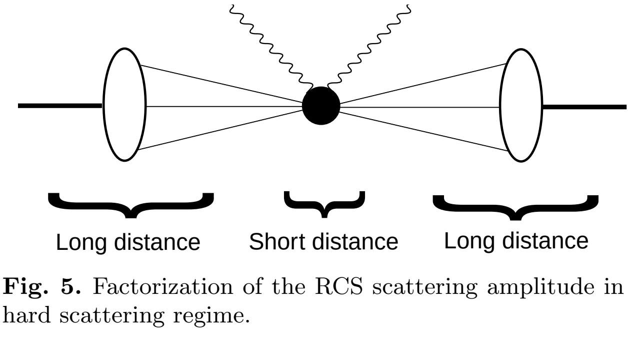

Fig. 5. Factorization of the RCS scattering amplitude in the hard scattering regime.

decreased. Therefore one expects a lack of coherence between the long-distance confining effects and the short-distance reaction. This incoherence between the soft and hard physics is the origin of the factorization which is illustrated in fig. 5.

4.2 Factorization and the nucleon distribution amplitude

The calculation of the RCS amplitude at large momentum transfer, follows the Brodsky-Lepage formalism [45], which leads to the factorized expression

$$T(\lambda', h'_{\mathrm{N}}, \lambda, h_{\mathrm{N}}) = \int \mathrm{d}x_i \, \mathrm{d}y_j \, \phi^*_{\mathrm{N}}(y_j) \, T_{\mathrm{H}}(\lambda', h'_{\mathrm{N}}, y_j, \lambda, h_{\mathrm{N}}, x_i; s, t) \, \phi_{\mathrm{N}}(x_i), \tag{37}$$

where $(x_i,\, y_i)$ are the momentum fractions of the quarks in the initial and final nucleon respectively, T_{H} is the hard-scattering kernel and ϕ_{N} is the distribution amplitude (DA). The evaluation of eq. (37) requires a four-fold convolution integral since there are two constraint equations ($x_1 + x_2 + x_3 = 1$ and $y_1 + y_2 + y_3 = 1$). In eq. (37) a sufficiently large momentum transfer is assumed in order to neglect the transverse-momentum dependence of the partons in the hard scattering amplitude T_{H}. In this limit, the integration over the transverse momenta $\mathbf{k}_{\perp i}$ (where $\sum_i \mathbf{k}_{\perp i} = \mathbf{0}$) acts only on the valence wave function

$$\Psi_{\mathrm{V}}(x_1, x_2, x_3; \mathbf{k}_{\perp 1}, \mathbf{k}_{\perp 2}, \mathbf{k}_{\perp 3}) \;, \tag{38}$$

which is the amplitude of the three quark state in the Fock expansion of the proton:

$$| \, P\rangle = \Psi_{\mathrm{V}} \mid qqq\rangle + \Psi_{\mathrm{q\bar{q}}} \mid qqq, q\bar{q}\rangle + \Psi_{\mathrm{g}} \mid qqq, g\rangle + ... \tag{39}$$

This valence wave function Ψ_{V} integrated up to a scale μ (which separates the soft and hard parts of the wave function) defines the DA which appears in eq. (37) :

$$\phi_{\mathrm{N}}(x_i, \mu) = \int^{\mu} \mathrm{d}^2\mathbf{k}_{\perp i} \; \Psi_{\mathrm{V}}(x_i; \mathbf{k}_{\perp i}) \; . \tag{40}$$

For μ much larger than the average value of the transverse momentum in the proton, this function ϕ_{N} depends only weakly on μ [45] and this dependence can be neglected.

The interest of the formalism is that the distribution amplitude is universal, that is independent of the particular reaction considered. Several distribution amplitudes have been modeled using QCD sum rules [46–48]. They have a characteristic shape and predict that in a proton, the u-quark with helicity along the proton helicity carries about 2/3 of its longitudinal momentum (see fig. 6).

For the computation of the hard scattering amplitude T_{H} (black circle in fig. 5), the leading-order PQCD contribution corresponds to the exchange of the minimum number of gluons (two in the present case) between the three quarks. The number of diagrams grows rapidly with the number of elementary particles involved in the reaction (42 diagrams for the nucleon form factor, 336 diagrams in the case of real or virtual Compton scattering). Despite the large number of diagrams, the calculation of T_{H} is a parameter free calculation once the scale $\Lambda_{\mathrm{QCD}} \approx 200$ MeV in the strong coupling $\alpha_{\mathrm{s}}(Q^2)$ is given. Note that configurations with more than three valence quarks are a priori allowed but since this implies the exchange of more hard gluons, the corresponding contribution is suppressed by powers of $1/t$.

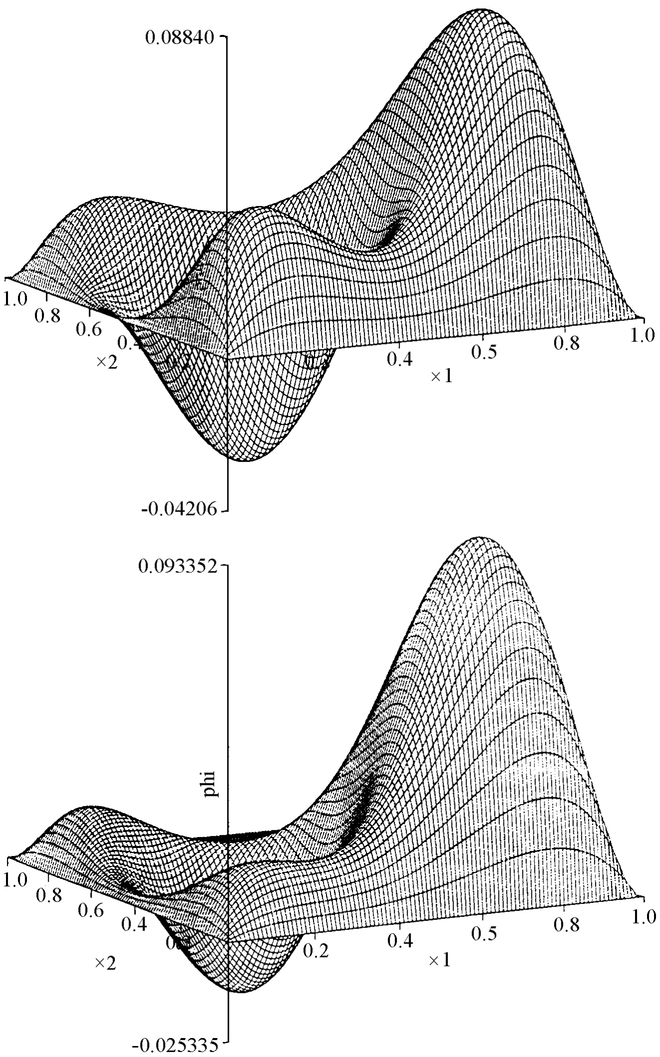

Fig. 6. Model distribution amplitudes for the nucleon : KS (upper figure) and COZ (lower figure), as a function of the valence quark momentum fractions x_1 and x_2 ($x_1 + x_2 + x_3 = 1$).

There are two characteristic features of the Brodsky-Lepage model which are almost direct consequences of QCD: the dimensional counting rules [49] and the conservation of hadronic helicities [50]. The latter feature implies that any helicity flip amplitude is zero and, hence, any single spin asymmetry too. The helicity sum rule is a consequence of utilizing the collinear approximation and of dealing with (almost) massless quarks which conserve their helicities when interacting with gluons. Whereas the dimensional counting rules are in reasonable agreement with experiment, the helicity sum rule seems to be violated even at moderately large momentum transfers. The prevailing opinion is that these phenomena cannot be explained in terms of perturbative QCD (see, for example, ref. [51]), but rather are generated by an interplay of perturbative and non-perturbative physics.

An interesting aspect of real and virtual Compton scattering is that these are the simplest processes in which the integrals over the longitudinal momentum fractions yield imaginary parts. The reason is that, as in any scattering process, there are kinematical regions where internal quarks and gluons can go on their mass shell. The appearance of imaginary parts to leading order in α_s is a non-trivial prediction of PQCD, which should be tested experimentally. As discussed in [1], the (e, e$'$ γ) reaction with polarized incoming electrons seems to be a good candidate for this investigation.

In contrast to the PQCD (or hard scattering) approach to RCS, it was argued in refs. [52,53] that wide angle Compton scattering at accessible energies is described by a competing mechanism, in which the large momentum transfer is absorbed on a single quark and shared by the overlap of high-momentum components in the soft wave function. This so-called soft-overlap mechanism gives a purely real amplitude, therefore displaying a different signature than the PQCD amplitude. The transition from such a soft-overlap mechanism to the perturbative, hard scattering approach when increasing the momentum transfer is an open question for a reaction such as wide angle Compton scattering (WACS). It is hoped that future experiments can shed light on this transition.

4.3 Results for RCS in PQCD

The leading-order PQCD prediction for RCS at large momentum transfer has been calculated several times in the literature [54–58].

The first step in such a calculation consists of evaluating the 336 diagrams entering the hard scattering amplitude T_{H} for RCS. Next, the four-fold convolution integral of eq. (37) has to be performed to obtain the Compton helicity amplitudes. The numerical integration requires some care because the quark and/or gluon propagators can go on-shell which leads to (integrable) singularities. The different numerical implementations of these singularities are probably the reason of the different results obtained in the literature.

In refs. [54,55], the propagator singularities were integrated by taking a finite value for the imaginary part $+i\epsilon$ of the propagator. The behavior of the result was then studied by decreasing the value of ϵ. To obtain convergence with a practical number of samples in the Monte Carlo integration performed in [54,55], the smallest feasible value for ϵ was $\epsilon \approx 0.005$. In ref. [56], the propagator singularities were integrated by decomposing the propagators into a principal value (off-shell) part and an on-shell part. Both methods were implemented and compared in ref. [57], and it was found that the $+i\epsilon$ method yields differences of the order of 10% for every diagram as compared with the result of the principal value method. It is not surprising that, when summing hundreds of diagrams, an error of 10% on every diagram can easily be amplified due to the interference between the diagrams.

To have confidence in the evaluation of the convolution of eq. (37), the principal value integration method was compared in ref. [57] with a third independent method. This third method starts from the observation that the diagrams can be classified into four categories depending upon the number of propagators which can develop singularities : in the present case this number is 0, 1, 2 or 3. Besides the trivial case of zero singularities which can be integrated immediately, the diagrams with one or two propagator singularities can be integrated by performing a contour integration in the complex plane for one of the four integrations. For the most difficult case of three propagator singularities, it was found to be possible to evaluate the diagram by performing two contour integrations in the complex plane. In doing so, one achieves quite a fast convergence because the integrations along the real axis are replaced by integrations along semi-circles in the complex plane which are far from the propagator poles. This method was compared with the principal value integration method, and the same results were found up to 0.1% for each type of singularity [57]. The principal value method was however found to converge much slower and is more complicated to implement, especially for the case with three singularities due to the coupled nature of the three principal value integrals.

Comparing the results of ref. [57] with those of ref. [56], a rather good agreement was found for all helicity amplitudes, except for the helicity amplitude where both photon and proton helicities are positive, in which case both calculations differ strongly. Very recently, the PQCD calculation for RCS at large momentum transfer has been recalculated again in ref. [58], by also performing convolution integrals through contour integrations in the complex plane. The authors of ref. [58] also find a strong difference with the results of [56] for the same helicity amplitude, where both photon and proton helicities are positive. Furthermore, in the angular region around 90°, where the PQCD formalism is supposed to be applicable, the authors of ref. [58] find a good agreement with the calculations of ref. [57], keeping in mind that there is an overall normalization uncertainty in these PQCD calculations for RCS, associated with α_s and the valence quark wave function normalization. The remaining difference between the results of refs. [57] and those of ref. [58] seems to be isolated to a single helicity amplitudes and appears for backward scattering angles. We therefore limit ourselves in the following discussion to the results in the angular region around 90° where the calculations of refs. [57] and [58] are in good agreement, and which is the most relevant

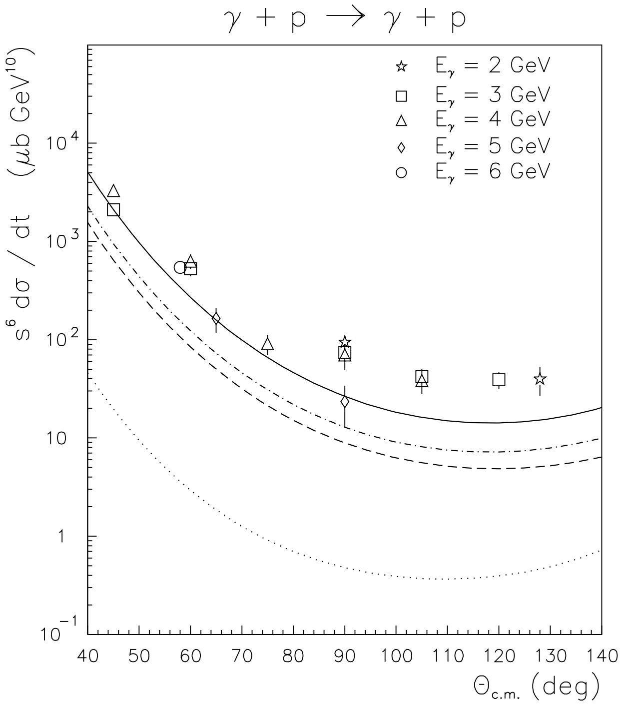

Fig. 7. Unpolarized Compton cross-section on the proton for different nucleon DA's : KS (full curve), COZ (dashed-dotted curve), CZ (dashed curve) and asymptotic DA (dotted curve). Calculations are from ref. [57], where also the references of the data can be found.

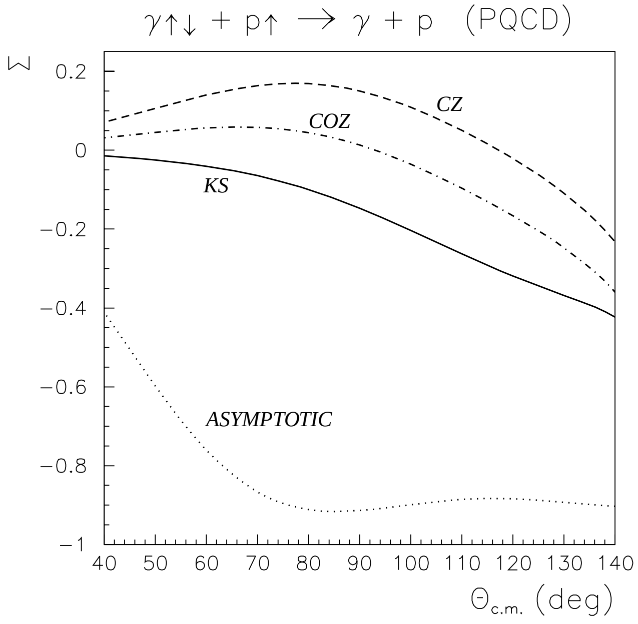

Fig. 8. PQCD calculations of the photon asymmetry on a polarized proton target for Compton scattering. Results (from ref. [57]) are shown for different DA's as indicated on the curves.

region for the PQCD calculation as it corresponds to the largest momentum transfer for a given photon energy.

In figs. 7 and 8, the PQCD calculations for RCS are shown for several model DA's denoted as CZ [46], COZ [47], KS [48], and the asymptotic DA.

The highest energy data which exist for real Compton scattering were taken around 5 GeV and are shown in fig. 7. Although the energy at which these experiments were performed is probably too low to justify a PQCD calculation, the comparison with these data is nevertheless shown in fig. 7 for illustrative purposes. The normalization of the calculations shown at these very low scales corresponds to using a frozen coupling constant, with $\alpha_s \approx 0.5$.

One first notices that the hard scattering amplitude for RCS has the s-dependence ($T \sim s^{-2}$) which leads to the QCD scaling laws [49], that is $\frac{d\sigma}{dt} \sim s^{-6}$ for Compton scattering or VCS. The unpolarized real Compton differential cross-section (multiplied by the scaling factor s^6) is shown in fig. 7 as function of the photon c.m. angle. It is observed that the result with the asymptotic DA ($\sim 120\, x_1 x_2 x_3$) is more than one decade below the results obtained with the amplitudes KS, COZ, and CZ, motivated by QCD sum rules. The results with KS, COZ and CZ show a similar characteristic angular dependence which is asymmetric around 90°. Note that in the forward and backward directions, which are dominated by diffractive mechanisms, a PQCD calculation is not reliable. Comparing the results obtained with KS, COZ and CZ, one notices that although these DA's have nearly the same lowest moments, they lead to differences of a factor of two in the Compton scattering cross-section. Consequently, this observable is sensitive enough to distinguish between various distribution amplitudes, provided, of course, one is in the regime where the hard scattering mechanism dominates.

In fig. 8, the polarized Compton cross-sections are shown for the two helicity states of the photon and for a target proton with positive helicity. One remarks that for all DA's there is a marked difference both in magnitude and angular dependence between the cross-sections for the two photon helicities. Consequently, the resulting photon asymmetry Σ, defined as

$$\Sigma_{\uparrow} = \frac{\frac{d\sigma}{dt}(\uparrow, \lambda = 1) - \frac{d\sigma}{dt}(\uparrow, \lambda = -1)}{\frac{d\sigma}{dt}(\uparrow, \lambda = 1) + \frac{d\sigma}{dt}(\uparrow, \lambda = -1)}, \tag{41}$$

where λ is the helicity of the incoming photon and $\uparrow$ denotes a positive hadron helicity, changes sign for the DA's KS, COZ, and CZ for different values of $\Theta_{\text{c.m.}}$ as shown in fig. 8. It is seen that the asymptotic DA on the other hand yields a very large, negative asymmetry around 90°. Therefore, it was suggested in ref. [57] that the photon asymmetry might be a particularly useful observable to distinguish between nucleon distribution amplitudes. The predicted sensitivity of the asymmetry to the nucleon DA can be used in the extraction of a DA from Compton scattering data in the scaling region. In ref. [57], a procedure was outlined to extract a DA from Compton data in a model independent way by first expanding the DA in a set of basis functions and then using the angular information of the cross-sections to fit the expansion coefficients. It was seen that the precision for these coefficients is greatly improved when one measures both unpolarized cross-sections and photon asymmetries.

A first dedicated experiment to measure the RCS differential cross-section and the asymmetry of eq. (41) for $\Theta_{\mathrm{c.m.}}$ around 90°, and for a real photon energy of 6 GeV, is planned at JLab [59]. In particular, it will be interesting to see if one approaches the PQCD result at these "lower" energies, and to study the interplay with soft-overlap type contributions for RCS as proposed in refs. [52,53].

It also remains to be investigated if corrections to the PQCD amplitudes are very process dependent when comparing form factors to a reaction as WACS. It was found unlikely in ref. [58] that the elastic proton form factors and WACS are both described by PQCD at accessible energies, which could imply large process dependent corrections to the PQCD amplitudes. It has further been shown in [58] that the PQCD and soft-overlap type mechanisms for WACS yield very different results for several polarization observables besides the asymmetry of eq. (41). Therefore such polarization observables have a great discriminatory potential in investigating the reaction mechanism at intermediate momentum transfers as compared with form factors.

At higher momentum transfers, RCS experiments using a real photon energy in the 15 GeV range, might be feasible, *e.g.*, at the HERA ring in the foreseeable future [60,61] and might open up prospects to study the nucleon valence wave function in a direct way.

5 Deeply virtual Compton scattering and skewed parton distributions

5.1 Introduction

Much of the internal structure of the nucleon has been revealed during the last two decades through the *inclusive* scattering of high-energy leptons on the nucleon in the Bjorken -or "Deep Inelastic Scattering" (DIS)-regime (where the photon virtuality Q^2 is very large, and $x_{\mathrm{B}} = Q^2/2p.q$ finite). *Unpolarized* DIS experiments have mapped out the quark and gluon distributions in the nucleon, while *polarized* DIS experiments have shown that only a small fraction of the nucleon spin is carried by the quarks. This has stimulated new investigations to understand the nucleon spin.

With the advent of the new generation of high-energy, high-luminosity lepton accelerators combined with large acceptance spectrometers, a wide variety of *exclusive* processes in the Bjorken regime are considered as experimentally accessible. In recent years, a unified theoretical description of such processes has emerged through a formalism introducing a new type of parton distributions, commonly denoted as skewed parton distributions (SPD's) [62–64]. These SPD's are generalizations of the parton distributions measured in DIS. It has been shown that these SPD's, which parametrize the structure of the nucleon, allow one to describe, in leading order perturbative QCD (PQCD), various exclusive processes in the near forward direction, where the momentum transfer to the nucleon is small. Such non-forward processes and the associated SPD's were already considered in the literature a longer time ago, see, *e.g.*, [65–69]. The most promising of these non-forward hard exclusive processes are deeply virtual Compton scattering (DVCS) and longitudinal electroproduction of vector or pseudoscalar mesons at large Q^2.

5.2 Definitions and modelizations of skewed parton distributions

The leading-order PQCD diagrams for DVCS and hard meson electroproduction are of the type as shown in fig. 9. The hard scale in fig. 9 is the photon virtuality Q^2, which should be large (of the order of several GeV^2), so as to be in the Bjorken regime. It has been proven [70,71] that the leading order DVCS amplitude in the forward direction can be factorized in a hard scattering part (which is exactly calculable in PQCD) and a soft, nonperturbative nucleon structure part as illustrated on the left panel of fig. 9. The nucleon structure information can be parametrized, at leading order, in terms of four (quark helicity conserving) generalized structure functions. These functions are the SPD's denoted by $H, \tilde{H}, E, \tilde{E}$ which depend upon three variables : x, ξ and t. The light-cone momentum [3] fraction x is defined by $k^+ = xP^+$, where k is the quark loop momentum and P is the average nucleon momentum ($P = (p + p')/2$, where $p(p')$ are the initial (final) nucleon four-momenta, respectively). The skewedness variable ξ is defined by $\Delta^+ = -2\xi\, P^+$, where $\Delta = p' - p$ is the overall momentum transfer in the process, and where $2\xi \to x_{\mathrm{B}}/(1 - x_{\mathrm{B}}/2)$ in the Bjorken limit. Furthermore, the third variable entering the SPD's is given by the Mandelstam invariant $t = \Delta^2$, being the total squared momentum transfer to the nucleon. In a frame where the virtual photon momentum q^μ and the average nucleon momentum P^μ are collinear along the z-axis and in opposite direction, one can parametrize the non-perturbative object in the lower blobs of fig. 9 as

$$\frac{P^+}{2\pi} \int \mathrm{d}y^- e^{ixP^+y^-} \langle p'|\bar{\psi}_\beta(-y/2)\psi_\alpha(y/2)|p\rangle \bigg|_{y^+=\mathbf{y}_\perp=0}$$

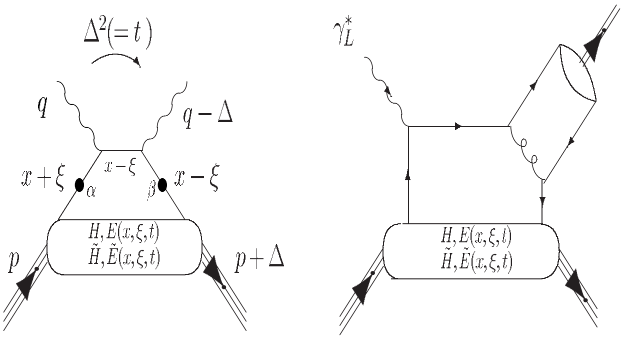

Fig. 9. Leading-order diagrams for DVCS (left) and for longitudinal electroproduction of mesons (right).

---

[3] Using the definition $a^\pm \equiv 1/\sqrt{2}(a^0 \pm a^3)$ for the light-cone components

$$= \frac{1}{4}\left\{(\gamma^-)_{\alpha\beta}\left[H^{\mathrm{q}}(x,\xi,t)\,\bar{N}(p^{'})\gamma^+N(p) + E^{\mathrm{q}}(x,\xi,t)\,\bar{N}(p^{'})i\sigma^{+\kappa}\frac{\Delta_\kappa}{2m_{\mathrm{N}}}N(p)\right] + (\gamma_5\gamma^-)_{\alpha\beta}\left[\tilde{H}^{\mathrm{q}}(x,\xi,t)\,\bar{N}(p^{'})\gamma^+\gamma_5N(p) + \tilde{E}^{\mathrm{q}}(x,\xi,t)\,\bar{N}(p^{'})\gamma_5\frac{\Delta^+}{2m_{\mathrm{N}}}N(p)\right]\right\}, \quad (42)$$

where ψ is the quark field, N the nucleon spinor and m_{N} the nucleon mass. The lhs of eq. (42) can be interpreted as a Fourier integral along the light-cone distance y^- of a quark-quark correlation function, representing the process where a quark is taken out of the initial nucleon (with momentum p) at the space-time point $y/2$, and is put back in the final nucleon (with momentum p') at the space-time point $-y/2$. This process takes place at equal light-cone time ($y^+ = 0$) and at zero transverse separation ($\mathbf{y}_\perp = 0$) between the quarks. The resulting one-dimensional Fourier integral along the light-cone distance y^- is with respect to the quark light-cone momentum xP^+. The rhs of eq. (42) parametrizes this non-perturbative object in terms of four SPD's, according to whether they correspond to a vector operator $(\gamma^-)_{\alpha\beta}$ or an axial-vector operator $(\gamma_5\gamma^-)_{\alpha\beta}$ at the quark level. The vector operator corresponds at the nucleon side to a vector transition (parametrized by the function H^{q}, for a quark of flavor q) and a tensor transition (parametrized by the function E^{q}). The axial-vector operator corresponds at the nucleon side to an axial-vector transition (function $\tilde{H}^{\mathrm{q}}$) and a pseudoscalar transition (function $\tilde{E}^{\mathrm{q}}$).

In fig. 9, the variable x runs from -1 to 1. Therefore, the momentum fractions ($x + \xi$ or $x - \xi$) of the active quarks can either be positive or negative. Since positive (negative) momentum fractions correspond to quarks (antiquarks), it has been noted in [63] that in this way, one can identify two regions for the SPD's : when $x > \xi$ both partons represent quarks, whereas for $x < -\xi$ both partons represent antiquarks. In these regions, the SPD's are the generalizations of the usual parton distributions from DIS. Actually, in the forward direction, the SPD's H and $\tilde{H}$ reduce to the quark density distribution $q(x)$ and quark helicity distribution $\Delta q(x)$ respectively, obtained from DIS :

$$H^{\mathrm{q}}(x,0,0) = q(x)\ , \qquad \tilde{H}^{\mathrm{q}}(x,0,0) = \Delta q(x)\ . \quad (43)$$

The functions E and $\tilde{E}$ are not measurable through DIS because the associated tensors in eq. (42) vanish in the forward limit ($\Delta \to 0$). Therefore, E and $\tilde{E}$ are new leading twist functions, which are accessible through the hard exclusive electroproduction reactions, discussed in the following.

In the region $-\xi < x < \xi$, one parton connected to the lower blob in fig. 9 represents a quark and the other one an antiquark. In this region, the SPD's behave like a meson distribution amplitude and contain completely new information about nucleon structure, because the region $-\xi < x < \xi$ is absent in DIS, which corresponds to the limit $\xi \to 0$.

Besides coinciding with the quark distributions at vanishing momentum transfer, the skewed parton distributions have interesting links with other nucleon structure quantities. The first moments of the SPD's are related to the elastic form factors (FF) of the nucleon through model independent sum rules. By integrating eq. (42) over x, one obtains the following relations for one quark flavor :

$$\begin{aligned}
\int_{-1}^{+1} \mathrm{d}x\, H^{\mathrm{q}}(x,\xi,t) &= F_1^{\mathrm{q}}(t)\,,\\
\int_{-1}^{+1} \mathrm{d}x\, E^{\mathrm{q}}(x,\xi,t) &= F_2^{\mathrm{q}}(t)\,,\\
\int_{-1}^{+1} \mathrm{d}x\, \tilde{H}^{\mathrm{q}}(x,\xi,t) &= g_{\mathrm{A}}^{\mathrm{q}}(t)\,,\\
\int_{-1}^{+1} \mathrm{d}x\, \tilde{E}^{\mathrm{q}}(x,\xi,t) &= h_{\mathrm{A}}^{\mathrm{q}}(t)\,.
\end{aligned} \quad (44)$$

The elastic FF for one quark flavor on the rhs of eqs. (44) are related to the physical ones (restricting oneself to u, d and s quark flavors) as

$$F_1^{\mathrm{u}} = 2F_1^{\mathrm{p}} + F_1^{\mathrm{n}} + F_1^{\mathrm{s}}\ , \qquad F_1^{\mathrm{d}} = 2F_1^{\mathrm{n}} + F_1^{\mathrm{p}} + F_1^{\mathrm{s}}\ , \quad (45)$$

where F_1^{p} and F_1^{n} are the usual proton and neutron Dirac FF respectively, and where F_1^{s} is the strangeness form factor. Relations similar to eq. (45) hold for the Pauli FF F_2^{q}. For the axial vector FF one uses the isospin decomposition :

$$g_{\mathrm{A}}^{\mathrm{u}} = \frac{1}{2}g_{\mathrm{A}} + \frac{1}{2}g_{\mathrm{A}}^0\ , \qquad g_{\mathrm{A}}^{\mathrm{d}} = -\frac{1}{2}g_{\mathrm{A}} + \frac{1}{2}g_{\mathrm{A}}^0\ , \quad (46)$$

where $g_{\mathrm{A}}(g_{\mathrm{A}}^0)$ are the isovector (isoscalar) axial FF respectively. Similar relations exist for h_{A}. The isovector axial form factor g_{A} is known from experiment, with $g_{\mathrm{A}}(0) \approx 1.267$. The induced pseudoscalar form factor h_{A} contains an important pion pole contribution, through the partial conservation of the axial current (PCAC).

A lot of the recent interest and activity in this field has been triggered by the observation of [62] that the SPD's may shed a new light on the "spin-puzzle". Starting from a (color) gauge-invariant decomposition of the nucleon spin : $1/2 = J_{\mathrm{q}} + J_{\mathrm{g}}$, where J_{q} and J_{g} are the total quark and gluon angular momentum, respectively, it was shown in [62] that the second moment of the unpolarized SPD's at $t = 0$ gives

$$J_{\mathrm{q}} = \frac{1}{2}\int_{-1}^{+1} \mathrm{d}x\, x\,\left[H^{\mathrm{q}}(x,\xi,t=0) + E^{\mathrm{q}}(x,\xi,t=0)\right], \quad (47)$$

and this relation is independent of ξ. The quark angular momentum J_{q} decomposes as : $J_{\mathrm{q}} = \Delta\Sigma/2 + L_{\mathrm{q}}$, where $\Delta\Sigma/2$ and L_{q} are the quark spin and orbital angular momentum, respectively. As $\Delta\Sigma$ is measured through polarized DIS experiments, a measurement of the sum rule of eq. (47) in terms of the SPD's, provides a model independent way to determine the quark orbital contribution L_q to the nucleon spin.

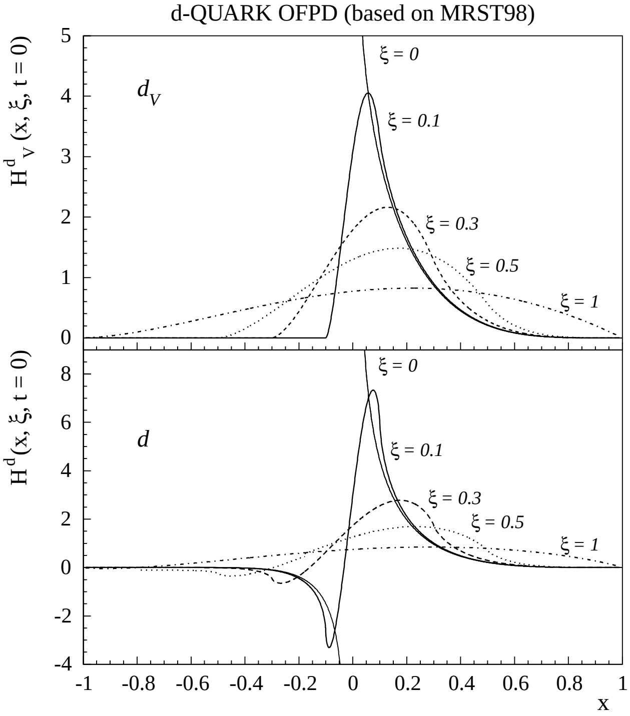

Fig. 10. ξ-dependence of the SPD H^{d} at $t = 0$ with the ansatz (based on the MRST98 [74] quark distributions) used in ref. [72]. Upper panel : valence d-quark SPD, lower panel : total d-quark SPD. The thin lines ($\xi = 0$) correspond with the ordinary d-quark distributions.

Ultimately, one wants to extract the SPD's from data, but in order to evaluate the electroproduction observables, and to study their sensitivity to the new physics, one needs an educated guess for the SPD's. In ref. [72], a model for the SPD's was constructed using a ξ-dependent product ansatz (for the double distributions of [69,73]) of a quark distribution and an asymptotic "meson-like" distribution amplitude (see ref. [72] for more details). For the quark distributions, the MRST98 parametrization [74] is used as input. The t-dependence of the model for the SPD's is given by the corresponding FF (Dirac form factor for H, axial form factor for $\tilde{H}$), so that the first moments of the SPD's are satisfied by construction. As an example, the d-quark SPD (formerly also denoted as off-forward parton distribution (OFPD)), using the above described ansatz, is shown in fig. 10.

One observes from fig. 10 the transition from a quark distribution ($\xi = 0$) to a meson distribution amplitude ($\xi = 1$). Model calculation of the SPD's are currently possible within the QCD chiral models for intermediate x_{B}. In particular, a calculation [75] in the chiral quark soliton model (see ref. [76] for a review) found a strong dependence of the SPD's on ξ and fast "crossovers" at $|x| = \xi$. Such behavior is related to the fact that the SPD's in the region $-\xi < x < \xi$ have properties of meson distribution amplitudes. In particular for the SPD H, this can be seen as being due to a scalar-isoscalar two-pion exchange contribution [77], indicating that the SPD's are qualitatively a richer source of nucleon structure information than ordinary parton distributions. One may expect that eventually it will be possible to calculate SPD's for intermediate x_{B} using lattice QCD.

5.3 Leading-order amplitudes and observables for DVCS and hard meson electroproduction

The leading-order (L.O.) DVCS amplitude in the forward direction is given [69,62] by the handbag diagram shown on the left panel of fig. 9 (the crossed diagram which is not shown is also understood). A formal factorization proof for DVCS has been given in [70,71].

To calculate the DVCS amplitude in the Bjorken regime, it is natural to express the momenta in the process (q^μ of the virtual photon, q'^μ of the real photon, and P^μ denoting the average nucleon momentum) in terms of the lightlike vectors

$$\tilde{p}^\mu = \frac{P^+}{\sqrt{2}}(1,0,0,1)\ , \qquad n^\mu = \frac{1}{P^+\sqrt{2}}(1,0,0,-1)\ . \qquad (48)$$

Using the parametrization of eq. (42) for the bilocal quark operator, the L.O. DVCS tensor $H^{\mu\nu}_{L.O.\,DVCS}$ (defined *e.g.*, in [1]) follows from the handbag diagrams as :

$$\begin{aligned}
& H^{\mu\nu}_{\mathrm{L.O.\,DVCS}} \\
&= \frac{1}{2}\left[\tilde{p}^\mu n^\nu + \tilde{p}^\nu n^\mu - g^{\mu\nu}\right] \\
&\quad \times \int_{-1}^{+1} \mathrm{d}x \left[\frac{1}{x-\xi+i\epsilon} + \frac{1}{x+\xi-i\epsilon}\right] \\
&\quad \times \Big[H^{\mathrm{p}}_{\mathrm{DVCS}}(x,\xi,t)\ \bar{N}(p^{'})\gamma.n N(p) \\
&\qquad + E^{\mathrm{p}}_{\mathrm{DVCS}}(x,\xi,t)\ \bar{N}(p^{'}) i\sigma^{\kappa\lambda}\frac{n_\kappa \Delta_\lambda}{2m_{\mathrm{N}}} N(p)\Big] \\
&+ \ \frac{1}{2}\left[-i\varepsilon^{\mu\nu\kappa\lambda}\tilde{p}_\kappa n_\lambda\right] \int_{-1}^{+1} \mathrm{d}x \left[\frac{1}{x-\xi+i\epsilon} - \frac{1}{x+\xi-i\epsilon}\right] \\
&\quad \times \Big[\tilde{H}^{\mathrm{p}}_{\mathrm{DVCS}}(x,\xi,t)\bar{N}(p^{'})\gamma.n\gamma_5 N(p) \\
&\qquad + \tilde{E}^{\mathrm{p}}_{\mathrm{DVCS}}(x,\xi,t)\bar{N}(p^{'})\gamma_5\frac{\Delta\cdot n}{2m_{\mathrm{N}}} N(p)\Big]\ . \qquad (49)
\end{aligned}$$

On the rhs of the DVCS tensor of eq. (49), the SPD's $H, \tilde{H}, E, \tilde{E}$ enter in a convolution integral over the quark momentum fraction x. This is a qualitative difference compared with DIS, where one is only sensitive (through the optical theorem) to the imaginary part of the forward double virtual Compton amplitude. We refer to ref. [1] for details and for the formalism to calculate DVCS observables starting from the DVCS tensor of eq. (49).

The leading-order DVCS amplitude corresponding to eq. (49), is exactly gauge invariant with respect to the virtual photon, *i.e.* $q_\nu\, H^{\mu\nu}_{\mathrm{L.O.\,DVCS}} = 0$. However, electromagnetic gauge invariance is violated by the real photon except in the forward direction. This violation of gauge invariance is a higher twist (twist-3) effect compared to the leading order term $H^{\mu\nu}_{\mathrm{L.O.\,DVCS}}$. Since $q^{'}_\mu\, H^{\mu\nu}_{L.O.DVCS} \sim$

$\Delta_\perp$, an improved DVCS amplitude linear in $\Delta_\perp$ has been proposed in ref. [1] to restore gauge invariance (in the nonforward direction) in a heuristic way :

$$H^{\mu\nu}_{\mathrm{DVCS}} = H^{\mu\nu}_{\mathrm{L.O.\,DVCS}} + \frac{\tilde{p}^{\mu}}{(\tilde{p}\cdot q')}\,(\Delta_\perp)_\lambda\, H^{\lambda\nu}_{\mathrm{L.O.\,DVCS}}\,, \tag{50}$$

leading to a correction term to the L.O. DVCS amplitude of order $O\,(\Delta_\perp/Q)$.

Very recently, the gauge invariance of the DVCS amplitude was addressed in much more detail in several works [78–80]. It was found that the twist-3 terms which restore gauge invariance (to twist-4 accuracy) involve two contributions. First there are terms proportional to the twist-2 SPD's of eq. (49), which were found to completely coincide with the improved DVCS amplitude of eq. (50). In addition, there are terms which are characterized by new 'transverse' SPD's (see refs. [78–80] for details). These latter functions are suppressed by one power $1/Q$ compared with the contribution of the twist-2 SPD's in DVCS cross-sections, and could in principle be separated by measuring DVCS observables over a sufficiently large Q^2 range (see, *e.g.*, [81] for tests of the handbag approximation to DVCS). In view of current DVCS experiments which are performed or planned at Q^2 in the few GeV^2 range only, the numerical importance of those additional contributions remains to be investigated.

Besides the DVCS process, a factorization proof was also given for the L.O. meson electroproduction amplitudes in the Bjorken regime [82,83], which is illustrated on the right panel of fig. 9. This factorization theorem only applies when the virtual photon is *longitudinally* polarized. In the valence region, the L.O. amplitude $\mathcal{M}^L$ for meson production by a longitudinal photon consists of evaluating fig. 9 (right panel, where only one of the four L.O. diagrams is shown) with the one-gluon exchange diagrams as hard scattering kernel. In this way, the L.O. expressions for ρ^0_{L} (longitudinally polarized vector meson) and π^0 electroproduction were calculated in [84] (see also ref. [85]) as

$$\begin{aligned}\mathcal{M}^L_{\rho^0_{\mathrm{L}}} &= -ie\,\frac{4}{9}\,\frac{1}{Q}\,\left[\int_0^1 \mathrm{d}z\frac{\Phi_\rho(z)}{z}\right]\\ &\times \frac{1}{2}\int_{-1}^{+1}\mathrm{d}x\left[\frac{1}{x-\xi+i\epsilon}+\frac{1}{x+\xi-i\epsilon}\right]\\ &\times (4\pi\alpha_s)\left\{H^{\mathrm{p}}_{\rho^0_{\mathrm{L}}}(x,\xi,t)\bar{N}(p')\gamma.nN(p)\right.\\ &\left.\qquad +E^{\mathrm{p}}_{\rho^0_{\mathrm{L}}}(x,\xi,t)\bar{N}(p')i\sigma^{\kappa\lambda}\frac{n_\kappa\Delta_\lambda}{2m_{\mathrm{N}}}N(p)\right\},\end{aligned} \tag{51}$$

$$\begin{aligned}\mathcal{M}^L_{\pi^0} &= -ie\,\frac{4}{9}\,\frac{1}{Q}\,\left[\int_0^1 \mathrm{d}z\frac{\Phi_\pi(z)}{z}\right]\\ &\times \frac{1}{2}\int_{-1}^{+1}\mathrm{d}x\left[\frac{1}{x-\xi+i\epsilon}+\frac{1}{x+\xi-i\epsilon}\right]\\ &\times (4\pi\alpha_s)\left\{\tilde{H}^{\mathrm{p}}_{\pi^0}(x,\xi,t)\bar{N}(p')\gamma.n\gamma_5N(p)\right.\\ &\left.\qquad +\tilde{E}^{\mathrm{p}}_{\pi^0}(x,\xi,t)\bar{N}(p')\gamma_5\frac{\Delta\cdot n}{2m_{\mathrm{N}}}N(p)\right\},\end{aligned} \tag{52}$$

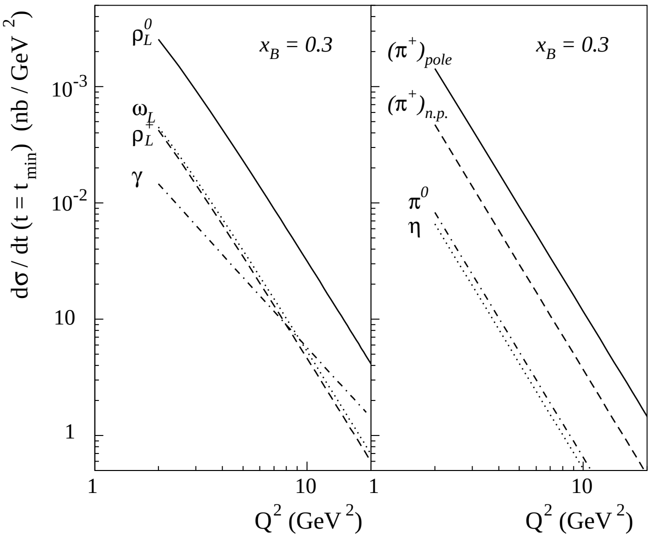

Fig. 11. Scaling behavior of the L.O. predictions for the forward differential electroproduction cross-section on the proton, for vector mesons (left panel) and pseudoscalar mesons (right panel), as calculated in ref. [72]. For the π^+ channel, the pion pole contribution (full curve, $(\pi^+)_{\mathrm{pole}}$) is shown separately from the $\tilde{H}$ contribution (dashed curve, $(\pi^+)_{\mathrm{n.p.}}$). The scaling behavior of the forward transverse L.O. DVCS cross-section is shown by the dashed-dotted curve in the left panel.

where α_{s} is the QCD coupling constant. Because the quark helicity is conserved in the hard scattering process, one finds the interesting result that the vector meson electroproduction amplitude depends only on the *unpolarized* SPD's H and E, whereas the pseudoscalar meson electroproduction amplitudes depend only on the *polarized* SPD's $\tilde{H}$ and $\tilde{E}$. In contrast, the DVCS amplitude of eq. (49) depends on both the unpolarized and polarized SPD's. Another difference from DVCS, is the fact that the meson electroproduction amplitudes require additional non-perturbative input from the meson distribution amplitudes $\Phi_\rho(z)$ and $\Phi_\pi(z)$ respectively, for which the asymptotic forms are taken in the calculations. From eqs. (51,52), one furthermore sees that the L.O. longitudinal amplitudes for meson electroproduction behave as $1/Q$. At large Q^2, fixed x_{B} and fixed t, this leads to a $1/Q^6$ behavior for the longitudinal cross section $\mathrm{d}\sigma_{\mathrm{L}}/\mathrm{d}t$, which provides an experimental signature (scaling) of the leading-order mechanism. Expressions analogous to eqs. (51, 52) have also been worked out for the charged meson channels $\rho^\pm, \pi^\pm$ as well as for the ω, ϕ and η channels (see refs. [86–88,72] for details).

According to the considered reaction, the SPD's enter in different combinations due to the charges and isospin factors. For DVCS on the proton, the combination is

$$H^{\mathrm{p}}_{\mathrm{DVCS}}(x,\xi,t) = \frac{4}{9}H^{\mathrm{u}} + \frac{1}{9}H^{\mathrm{d}} + \frac{1}{9}H^{\mathrm{s}}\,, \tag{53}$$

and similarly for $\tilde{H}$, E and $\tilde{E}$. For electroproduction of ρ^0 and π^0 on the proton, the isospin structure yields the

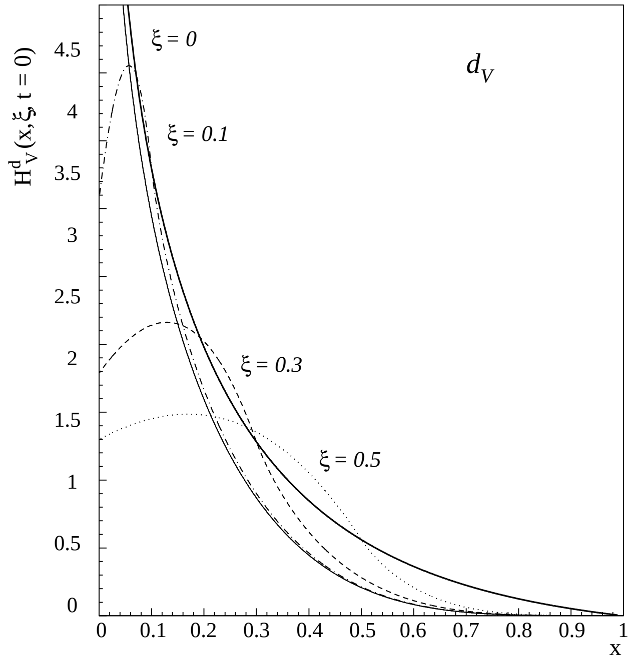

Fig. 12. Valence d-quark contribution to the SPD $H^{\rm d}$ at $t = 0$ for different values of ξ as indicated on the curves, calculated with the ansatz as in fig. 10. The thin (lower) solid curve ($\xi = 0$) corresponds to the ordinary d-quark distributions, whereas the thick (upper) solid curve to the envelope function $H_V^{\rm d}(x = \xi, \xi, t = 0)$ as measured through the SSA.

combination

$$H^{\rm p}_{\rho^0}(x,\xi,t) = \frac{1}{\sqrt{2}}\left\{\frac{2}{3}H^{\rm u} + \frac{1}{3}H^{\rm d}\right\}, \tag{54}$$

$$\tilde{H}^{\rm p}_{\pi^0}(x,\xi,t) = \frac{1}{\sqrt{2}}\left\{\frac{2}{3}\tilde{H}^{\rm u} + \frac{1}{3}\tilde{H}^{\rm d}\right\}, \tag{55}$$

and similar for E and $\tilde{E}$. Corresponding relations for the $\rho^\pm, \omega, \phi, \pi^\pm$ and η channels can be found in refs. [86–88, 72]. Therefore, the measurements of the different meson production channels are sensitive to different combinations of the same universal SPD's, and allow us to perform a flavor separation of the SPD's, provided one is able to deconvolute the SPD's from the leading-order amplitudes.

Some representative results for DVCS and meson electroproduction observables using the ξ-dependent ansatz for the SPD's, are shown in the following. More detailed results can be found in refs. [84,1,72].

Before considering the extraction of the SPD's from electroproduction data, it is compulsory to demonstrate that the scaling regime has been reached. In fig. 11, the forward longitudinal electroproduction cross-sections are shown as a function of Q^2 and the L.O. predictions are compared for different mesons. The L.O. amplitude for longitudinal electroproduction of mesons was seen to behave as $1/Q$, leading to a $1/Q^6$ scaling behavior for $d\sigma_{\rm L}/dt$.

By comparing the different vector meson channels in fig. 11, one sees that the $\rho^0_{\rm L}$ channel yields the largest cross-section. The $\omega_{\rm L}$ channel in the valence region ($x_{\rm B} \approx 0.3$) is about a factor of 5 smaller than the $\rho^0_{\rm L}$ channel, which is to be compared with the ratio at small $x_{\rm B}$ (in the diffractive regime) where $\rho^0 : \omega = 9 : 1$. The $\rho^+_{\rm L}$ channel, which is sensitive to the isovector combination of the unpolarized SPD's, yields a cross-section comparable to the $\omega_{\rm L}$ channel. The $\rho^+_{\rm L}$ channel is interesting as there is no competing diffractive contribution, and therefore allows to test directly the quark SPD's. The three vector meson channels ($\rho^0_{\rm L}$, $\rho^+_{\rm L}$, $\omega_{\rm L}$) are highly complementary in order to perform a flavor separation of the unpolarized SPD's $H^{\rm u}$ and $H^{\rm d}$. A dedicated experiment is planned at JLab at 6 GeV in the near future [89] to investigate the onset of the scaling behavior for $\rho^0_{\rm L}$ electroproduction in the valence region ($Q^2 \approx 3.5$ GeV^2, $x_{\rm B} \approx 0.3$).

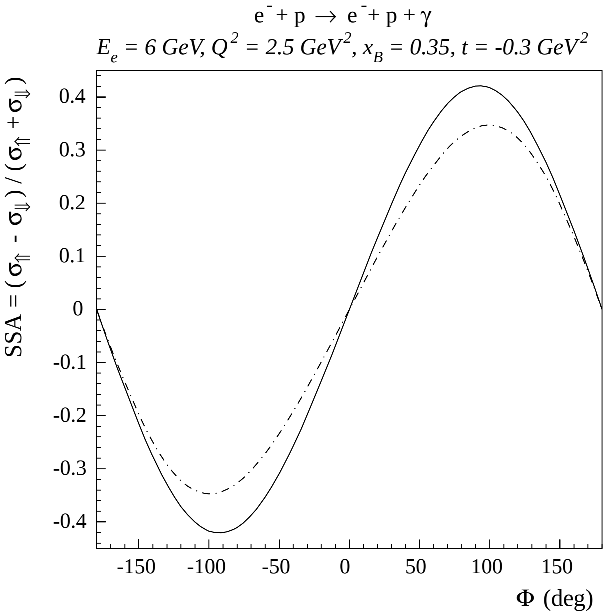

Fig. 13. A comparison of the single spin asymmetries for DVCS in JLab kinematics, for a ξ-independent ansatz for the SPD's as in ref. [1] (dashed-dotted curve), and a ξ-dependent ansatz for the SPD's as in fig. 10 (full curve).

For the pseudoscalar mesons which involve the polarized SPD's, one remarks in fig. 11 the prominent contribution of the charged pion pole to the π^+ cross-section. For the contribution proportional to the SPD $\tilde{H}$, it is also seen that the π^0 channel is about a factor of 5 below the π^+ channel due to isospin factors. In the π^0 channel, the u- and d-quark polarized SPD's enter with the same sign, whereas in the π^+ channel, they enter with opposite signs. As the polarized SPD's are constructed here from the corresponding polarized parton distributions, the difference between the predictions for the π^0 and π^+ channels results from the fact that the polarized d-quark distribution is opposite in sign to the polarized u-quark distribution. For the η channel, the ansatz for the SPD $\tilde{H}$ based on the polarized quark distributions yields a prediction comparable to the π^0 cross-section.

For the γ leptoproduction in the few GeV beam energy range, the cross-section is dominated by the Bethe-Heitler (BH) process (see ref. [1]). However, it was suggested in ref. [1] that an exploration of DVCS might be possible if the beam is polarized. The electron single spin asymmetry (SSA) does not vanish out of plane due to the interference between the purely real BH process and the imaginary part of the DVCS amplitude. Because the SSA measures the imaginary part of the DVCS amplitude, it is directly proportional to a linear combination of the SPD's along the line $x = \xi$. In fact, the SSA maps out an 'envelope' function, *e.g.*, $H(x = \xi, \xi, t)$, as shown, *e.g.*, in fig. 12 for the valence down quark SPD in the ansatz of fig. 10.

In fig. 13, it is shown that the SSA yields a sizeable asymmetry for JLab kinematics, and displays a sensitivity to the ξ-dependent shape of the SPD's. An experiment to measure the SSA for DVCS is planned at JLab at 6 GeV [90]. The SSA for DVCS is at present also measured at HERMES [91].

Going up in energy, the increasing virtual photon flux factor boosts the DVCS part of the γ leptoproduction cross-section, making it more important compared to the BH contribution. This provides a nice opportunity for COMPASS at 200 GeV beam energy, where experiments have been proposed for DVCS [92] and meson electroproduction [93].

5.4 Extension to hard exclusive electroproduction of decuplet baryons

In the previous section, the main focus were the reactions $\gamma^* + \mathrm{N} \to \gamma + \mathrm{N}'$ and $\gamma^*_{\mathrm{L}} + \mathrm{N} \to \mathrm{M} + \mathrm{N}'$ with M a meson, and where N′ is an octet baryon. One of the intriguing questions of medium-energy QCD dynamics is the differences and similarities in the structure of baryons belonging to the different $SU(3)_{\mathrm{f}}$ multiplets. In particular, a naive constituent quark model predicts that they are similar, while there are suggestions that due to a strong attraction between the quarks in the spin-isospin zero channel, diquark correlations should be important in the baryon octet but not in the decuplet [94]. At the same time the chiral models suggest that in the limit of a large number of colors (large N_{c}) of QCD, which is known to be a useful guideline, nucleons and Δ isobars are different rotational excitations of the same soliton [95,96].

For these studies, the potential of the process $\gamma^*_{\mathrm{L}} + \mathrm{N} \to \pi + \Delta$ as well as the DVCS process $\gamma^* + \mathrm{N} \to \gamma + \Delta$, was explored in ref. [97]. In addition, the study of the processes with production of decuplet baryons has also a practical usefulness, because in the experiments with low resolution in the mass of the recoiling system ($\Delta M \approx 300$ MeV for HERMES in the current set-up), the estimates of Δ production are necessary to extract the N → N SPD's from such data.

In ref. [97], a new set of SPD's were introduced for the axial N → Δ (isovector) transition, denoted as $C_i^{(3)}$, which enter into $\pi\Delta$ electroproduction :

$$\frac{P^+}{2\pi}\int \mathrm{d}y^- e^{ixP^+y^-}\left.\langle \Delta^+|\bar{\psi}(-y/2)\not{n}\gamma^5\psi(y/2)|N\rangle\right|_{y^+=\mathbf{y}_\perp=0}$$
$$= \bar{\psi}^\beta(p')\,\left[C_1^{(3)}(x,\xi,t)\,n_\beta + C_2^{(3)}(x,\xi,t)\,\frac{\Delta_\beta(n\cdot\Delta)}{m_{\mathrm{N}}^2} + \dots\right]N(p), \qquad (56)$$

where the same notations are used as before, and where $\psi^\beta(p')$ is the Rarita-Schwinger spinor for the Δ isobar. In eq. (56), the ellipses denote other contributions which are suppressed at large N_{c}. For the N → Δ DVCS process, besides the axial SPD's, also vector SPD's enter which were also defined in ref. [97].

The observation that in the large-N_{c} limit, the nucleon and Δ are rotational excitations of *the same* classical soliton object, allows us to derive a number of relations between N → N and N → Δ SPD's. For $C_1^{(3)}$ and $C_2^{(3)}$, these have the form [86] :

$$C_1^{(3)}(x,\xi,t) = \sqrt{3}\,\widetilde{H}^{(3)}(x,\xi,t), \qquad (57)$$

$$C_2^{(3)}(x,\xi,t) = \sqrt{3}/4\,\widetilde{E}^{(3)}(x,\xi,t)\,, \qquad (58)$$

in terms of the (isovector) N → N SPD $\widetilde{H}^{(3)} = \widetilde{H}^{\mathrm{u}} - \widetilde{H}^{\mathrm{d}}$, and analogously for $\widetilde{E}^{(3)}$.

Using the large-N_{c} relations of eq. (57), one can easily derive the relations between the different cross-sections for charged pion production as $\sigma_{\mathrm{L}}^{\gamma^*\mathrm{p}\to\pi^+\mathrm{n}} : \sigma_{\mathrm{L}}^{\gamma^*\mathrm{p}\to\pi^+\Delta^0} : \sigma_{\mathrm{L}}^{\gamma^*\mathrm{p}\to\pi^-\Delta^{++}} : \sigma_{\mathrm{L}}^{\gamma^*\mathrm{n}\to\pi^-\mathrm{p}} \approx 1 : 0.5 : 1.25 : 0.8$.

Besides the cross-section σ_{L}, the second observable involving only longitudinal amplitudes and being a leading-order observable for hard exclusive meson electroproduction, is the single spin asymmetry, for a proton target polarized perpendicular to the reaction plane (or the equivalent recoil polarization observable) [86]. These transverse spin asymmetries for π^+n and $\pi^+\Delta^0$ are shown in fig. 14.

It is obvious from fig. 14, that large transverse spin asymmetries are predicted for these processes, related to

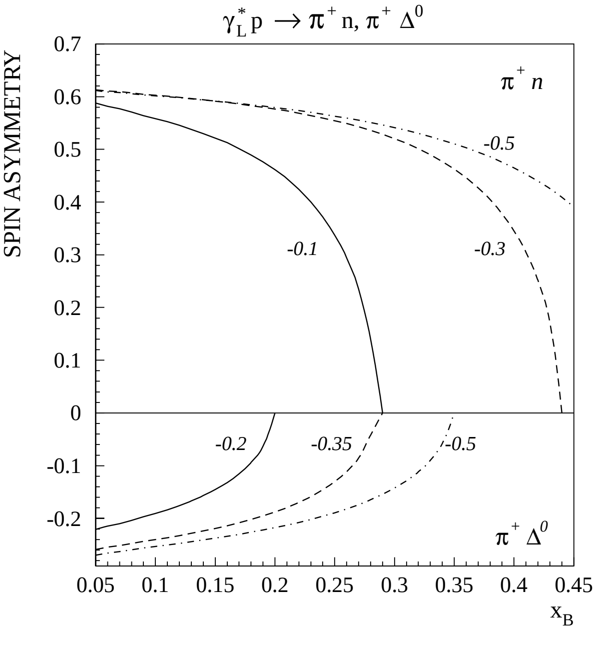

Fig. 14. Transverse spin asymmetries for the longitudinal electroproduction of π^+n and $\pi^+\Delta^0$, at different values of t (in (GeV/c)^2). Figure from ref. [97].

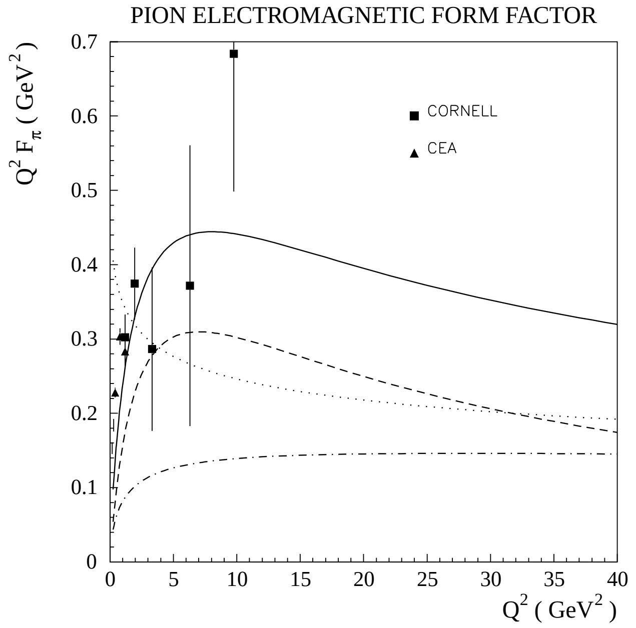

Fig. 15. Results for the π electromagnetic form factor of the leading-order PQCD prediction without (dotted line) and with (dashed-dotted line) inclusion of the corrections due to intrinsic transverse momentum dependence. The dashed curve shows the result for the soft overlap contribution and the total result (full line) is the sum of the dashed and dashed-dotted lines. Figure from ref. [72], where the references of the data can also be found.

the peculiar feature of chiral QCD. As a consequence, investigations of these processes can provide unique tests of the soliton type approach to baryon structure. The spin asymmetries are likely to be less sensitive to higher twist effects and hence can be explored already using the HERMES detector and JLab at higher energies. Furthermore, the study of these processes would allow one to make a more reliable separation of the π pole contribution in the electroproduction of pions, which is mandatory for the measurement of the pion elastic form factor at higher Q^2.

5.5 Power corrections to the leading-order amplitudes

When measuring hard electroproduction reactions in the region $Q^2 \approx 1 - 20$ GeV^2, there arises the question of the importance of power corrections to the leading-order amplitudes, *i.e.* how fast does one approach the scaling regime predicted by the L.O. amplitudes. One source of power corrections is evident from the structure of the matrix element of eq. (42) which defines the SPD's, where the quarks are taken at zero transverse separation. This amounts to neglect, at leading order, the quark's transverse momentum compared with its large longitudinal (+ component) momentum. A first estimate of these corrections due to the quark's intrinsic transverse momentum has been obtained in ref. [72], which is referred to for details. This correction is known to be important for a successful description at the lower Q^2 values of the $\pi^0\gamma^*\gamma$ transition FF, for which data exist in the range $Q^2 \approx 1-10$ GeV^2. For the pion elastic FF in the transition region before asymptotia is reached, the power corrections due to both the transverse momentum dependence and the soft overlap mechanism (*i.e.* the process which does not proceed through one-gluon exchange) are quantitatively important. The result for the pion elastic FF is shown in fig. 15, where it is seen that the leading-order PQCD result is approached only at very large Q^2. The correction including the transverse momentum dependence gives a substantial suppression at lower Q^2 (about a factor of two around $Q^2 \approx 5$ GeV^2). At these lower Q^2 values, the inclusion of the transverse momentum dependence renders the PQCD calculation internally consistent.

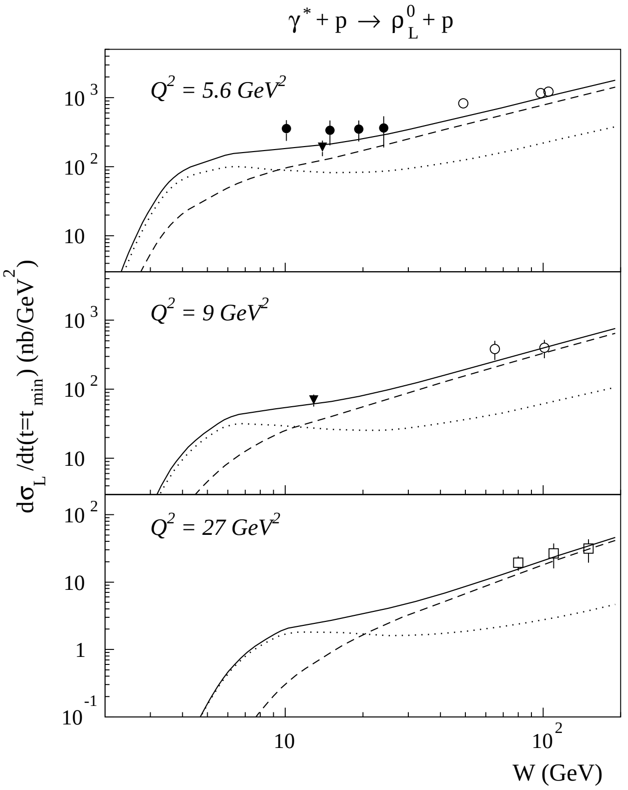

Fig. 16. Longitudinal forward differential cross-section for ρ^0_L electroproduction. Calculations compare the quark exchange mechanism (dotted lines) with the two-gluon exchange mechanism (dashed lines) and the sum of both (full lines). Both calculations include the corrections due to intrinsic transverse momentum dependence. The data are from NMC (triangles), E665 (solid circles), ZEUS 93 (open circles) and ZEUS 95 (open squares). Figure from ref. [72], where the references of the data can also be found.

These form factors were taken as a guide in ref. [72] to estimate the corrections due to the parton's intrinsic transverse momentum dependence in the DVCS and hard meson electroproduction amplitudes.

Although experimental data for ρ^0_L electroproduction at larger Q^2 do not yet exist in the valence region ($x_B \approx 0.3$), the reaction $\gamma^*_L\,p \longrightarrow \rho^0_L\,p$ has been measured at smaller values of x_B. Therefore, in fig. 16 the calculations are compared to those data, in order to study how the valence region is approached, in which one is sensitive to the quark SPD's. For the purpose of this discussion, we call the mechanism proceeding through the quark SPD's (*i.e.* the right panel of fig. 9), the Quark Exchange Mechanism (QEM). Besides the QEM, ρ^0 electroproduction at large Q^2 and small x_{B} proceeds predominantly through a perturbative two-gluon exchange mechanism (PTGEM) as studied in ref. [98]. To compare to the data at intermediate Q^2, the power corrections due to the parton's intrinsic transverse momentum dependence were implemented in both mechanisms (see ref. [72] for details), which gives a significant reduction at the lower Q^2. The results are compared with the data in fig. 16, showing that the PTGEM explains well the fast increase of the cross-section at high c.m. energy (W), but substantially underestimates the data at the lower energies. This is where the QEM is expected to contribute since x_{B} is then in the valence region. The results including the QEM describe the change of behavior of the data at lower W quite nicely.

Recently, ρ^0_{L} data have been obtained by the HERMES Collaboration for Q^2 up to 5 GeV^2 and around $W \approx$ 5 GeV [99]. These data show a clear dominance of the QEM in the intermediate W range as predicted in [84, 72]. The model ansatz for the SPD's of ref. [72] gives a fairly good agreement with these longitudinal ρ^0 electroproduction data [99].

5.6 Perspectives and outlook

In order to extract SPD's from forthcoming data, the Q^2 evolution of the SPD's has been worked out at the next-to-leading-order (NLO) level in ref. [100], which shows that the Q^2 evolution of the SPD's interpolates between the evolution of parton distributions and the evolution of distribution amplitudes. The NLO α_{s} corrections to the DVCS hard scattering amplitude have been calculated in refs. [101,70]. A NLO calculation of the DVCS amplitude in the region $x_{\mathrm{B}} > 10^{-2}$, including the two-loop evolution effects of the SPD's has been performed recently in ref. [102], to which we refer for details.

A major open theoretical question in this field is how the SPD's can be deconvoluted from the leading-order amplitudes. Suitable parametrizations of the SPD's, incorporating all physical constraints, might be one avenue to tackle this problem. In the absence of a solution to this problem, one has to resort to model calculations or educated guesses for the SPD's in order to compare with the data.

On the experimental side, it is clear that new and accurate data are needed for various exclusive channels at large Q^2 in the valence region, where the quark exchange mechanism dominates. Several experiments are being performed or are planned or proposed at JLab [89,103,90], HERMES and COMPASS [93,92]. Looking somewhat further into the future, the measurement of hard exclusive reactions will be one of the central themes for the planned upgrade of JLab to 12 GeV [104]. A facility with high luminosity combined with an intermediate energy of around 25 GeV, such as, *e.g.*, the ELFE project [105], will be a dedicated facility to measure these exclusive reactions at high momentum transfer and to map out these new SPD's in detail. Although such exclusive experiments at large Q^2 are quite demanding, the fundamental interest of the SPD's justifies an effort towards their experimental determination.

6 QED radiative corrections to virtual Compton scattering

6.1 Introduction

We have discussed in section 3 how VCS below pion production threshold, allows us to access generalized polarizabilities of the proton. Furthermore, we have seen in section 5 that VCS in the Bjorken regime determines generalized parton distributions of the nucleon. In both regimes, experiments are either being done or planned for the near future. In order to extract the nucleon structure information of interest from the ep → epγ reaction, especially in those kinematical situations where the Bethe-Heitler process is not negligible, it is indispensable to have a very good understanding of the QED radiative corrections to the ep → epγ reaction.

The ep → epγ reaction is particular in comparison with other electron scattering reactions, because the photon can be emitted from both the proton side (this is the VCS process which contains the nucleon structure information of interest) or from one of the electrons (which is the Bethe-Heitler process). The radiative corrections obtained from the Bethe-Heitler process differ formally from the case of elastic electron scattering.

6.2 Results for the QED radiative corrections to VCS

The first order QED radiative corrections to the ep → epγ reaction were calculated in ref. [106]. The one-loop virtual radiative corrections have been evaluated by a combined analytical-numerical method. Several tests were performed to cross-check the numerical method used. It was shown in ref. [106] how all IR divergences cancel when adding the soft-photon emission processes. Furthermore, a fully numerical method was presented for the photon emission processes where the photon energy is not very small compared with the electron energies, which makes up the radiative tail.

Figure 17 shows as representative result the effect of the radiative corrections on the VCS differential cross section for the MAMI VCS experiment [31] at an outgoing photon energy of $\mathrm{q}' = 111.5$ MeV (we refer to [106] for all details and more results). It is seen that the total effect of the radiative corrections in these kinematics is a reduction of the BH+Born cross-section of the order of 20%. The effect of the radiative corrections was also confirmed by the experimental results at very low energy of the outgoing photon ($\mathrm{q}' = 33$ MeV), where the effect of the GP's

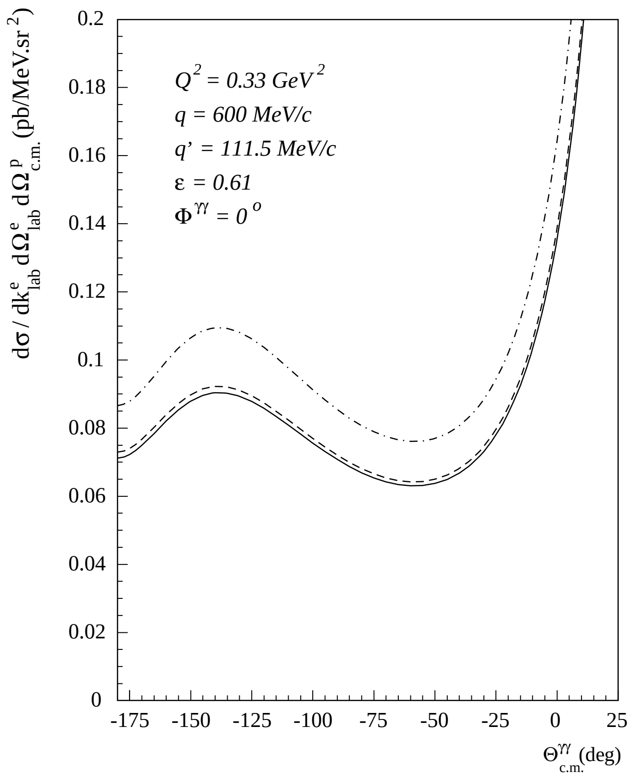

Fig. 17. Differential ep → epγ cross-section for MAMI kinematics at q' = 111.5 MeV/c. Dashed-dotted curve : BH + Born contribution, dashed curve : BH + Born + virtual radiative correction, full curve : BH + Born + total radiative correction. Figure from ref. [106].

is negligible. From the difference between the radiatively corrected data and the BH + Born result, the two values of eq. (25) for the combinations of the proton's GP's at $Q^2 \simeq 0.33$ GeV^2 have been extracted in ref. [31].

In ref. [106], calculations of the VCS radiative corrections were also given for unpolarized and polarized VCS observables both at low energies and in the Bjorken regime. The results will be an important tool for the analysis of present and forthcoming VCS experiments, in order to extract the nucleon structure information from these experiments.

7 Conclusions and outlook

It has been discussed how the real and virtual Compton scattering in different kinematical regimes provide new tools to extract nucleon structure information.

It has been seen that for RCS at low energy, new accurate data have become available which not only allow the extraction of scalar polarizabilities of the proton, but also start to explore the spin polarizabilities of the nucleon. Those spin polarizabilities have been calculated recently to $O(p^4)$ in HBChPT. A fixed-t dispersion relation formalism was developed to extract the nucleon polarizabilities with a minimum of model dependence from both unpolarized and polarized RCS data. The DR formalism was also used to obtain information on new higher-order polarizabilities of the proton, providing new nucleon structure observables and a new testing ground for the chiral calculations.

The VCS reaction at low photon energy maps out the spatial distribution of the polarization densities of the proton, through generalized polarizabilities. Over the last few years, the VCS has become a mature field and a first experiment at MAMI at low energy has been successfully completed. In order to extract GP's from VCS data over a larger range of energies, a dispersion relation formalism is underway, providing a new tool to analyze such data. The DR formalism provides already results for 4 of the 6 GP's, which can be confronted with chiral predictions.

The RCS reaction at high-energy and large-momentum transfer is a tool to access information on the partonic structure of the nucleon. The PQCD predictions for wide angle real Compton scattering (90° in the c.m.) show a strikingly different behavior than competing soft-overlap type mechanisms, and forthcoming experiments can teach us about the interplay of both mechanism at accessible energies.

The VCS reaction in the Bjorken regime and associated hard electroproduction reactions give access to new, generalized (skewed) parton distributions. The study of SPD's has opened up a whole new field in the study of nucleon structure. These observables unify two different fields as they interpolate between purely inclusive quantities (parton distributions) on the one hand and between simple exclusive quantities (such as form factors) on the other hand. Besides the SPD's H and $\tilde{H}$, which reduce in the DIS limit to the quark distribution and quark helicity distribution respectively, there are two entirely new leading twist SPD's (E and $\tilde{E}$), which cannot be accessed in DIS. The non-perturbative information contained in the SPD's is rather rich as they are functions of 3 different variables. In particular, the skewedness variable ξ leads to different regions where one is sensitive either to quark distribution type information or to meson distribution amplitude information in the nucleon. Through a sum rule, two of these SPD's (H and E) determine the quark orbital angular momentum contribution to the nucleon spin. An educated guess was shown for these SPD's, which was used to estimate the leading-order DVCS amplitude. Furthermore, the leading-order meson electroproduction amplitudes were discussed and compared to the available data. In particular it was seen that in the intermediate W range (valence region), a dominance of the handbag mechanism is predicted for ρ^0 electroproduction, which seems to be well confirmed by recent HERMES data. Furthermore, the extension of the formalism of the SPD's to the N → Δ transition was discussed. The large-N_c limit allows to relate the N → Δ SPD's to the N → N SPD's. The transverse spin asymmetry was discussed as a promising observable, likely to be less sensitive to higher twist effects.

It is easy to foresee that the fields of real and virtual Compton scattering will show important activities in the near future both on the theoretical and experimental sides, and that an attempt to review them is very timely. It is hoped however, that the works initiated and discussed in this paper will stimulate further efforts on the theoretical and experimental sides to extend our knowledge of nucleon structure in new directions.

It is a pleasure for me to thank my collaborators who participated in an important way in the different works referred to in this paper : N. D'Hose, D. Drechsel, L.L. Frankfurt, J.M. Friedrich, M. Gorchtein, P.A.M. Guichon, M. Guidal, B. Holstein, D. Lhuillier, D. Marchand, A. Metz, B. Pasquini, M.V. Polyakov, M. Strikman, L. Van Hoorebeke, and J. Van de Wiele. I also like to thank the many experimental colleagues working in these fields for numerous and very useful discussions. Furthermore, I would like to thank D. Drechsel also for a careful reading of the text. This work was supported by the Deutsche Forschungsgemeinschaft (SFB443).

References

1. Guichon P.A.M. and M. Vanderhaeghen, Prog. Part. Nucl. Phys. **41**, 125 (1998).
2. L'vov A., V.A. Petrun'kin and M. Schumacher, Phys. Rev. C **55**, 359 (1997).
3. MacGibbon B.E., G. Garino, M.A. Lucas, A.M. Nathan, G. Feldman and B. Dolbilkin, Phys. Rev. C **52**, 2097 (1995).
4. Olmos de Léon V., Ph.D. thesis, University Mainz, 2000.
5. Baldin A.M., Nucl. Phys. **18**, 310 (1960); L.I. Lapidus, Sov. Phys. JETP **16**, 964 (1963).
6. Damashek M. and F.J. Gilman, Phys. Rev. D **1**, 1319 (1970).
7. Babusci D., G. Giordano and G. Matone, Phys. Rev. C **57**, 291 (1998).
8. Sandorfi A.M., C.S. Whisnant and M. Khandaker, Phys. Rev. D **50**, R6681 (1994).
9. Drechsel D., M. Gorchtein, B. Pasquini, and M. Vanderhaeghen, Phys. Rev. C **61**, 015204 (2000).
10. Arends H.J., in *Proceedings of the XVI International Conference on Few-Body Problems in Physics, Taipei, Taiwan, 6-10 March 2000.* To appear in Nucl. Phys. A.
11. Hanstein O., D. Drechsel, L. Tiator, Nucl. Phys. A **632**, 561 (1998).
12. Arndt R.A., I.I. Strakovsky and R.L. Workman, Phys. Rev. C **53**, 430 (1996).
13. Tonnison J., A.M. Sandorfi, S. Hoblit and A.M. Nathan, Phys. Rev. Lett. **80**, 4382 (1998).
14. Bernard V., N. Kaiser, A. Schmidt, U.-G. Meissner, Phys. Lett. B **319**, 269 (1993); Z. Phys. A **348**, 317 (1994).
15. Hemmert T.R., B.R. Holstein, and J. Kambor, Phys. Rev. D **55**, 5598 (1997).
16. Hemmert T.R., B.R. Holstein, J. Kambor and G. Knöchlein, Phys. Rev. D **57**, 5746 (1998).
17. Ji X., C.-W. Kao, and J. Osborne, Phys. Rev. D **61**, 074003 (2000).
18. Vijaya Kumar K.B., J.A. McGovern, and M.C. Birse, Phys. Lett. B **479**, 167 (2000).
19. Gellas G.C., T.R. Hemmert, and U. Meissner, Phys. Rev. Lett. **85**, 14 (2000).
20. Drechsel D., M. Gorchtein, B. Pasquini, and M. Vanderhaeghen, in preparation.
21. Wissmann F. et al., Nucl. Phys. **A 660**, 232 (1999).
22. Holstein B.R., D. Drechsel, B. Pasquini, and M. Vanderhaeghen, Phys. Rev. C **61**, 034316 (2000).
23. Hemmert T.R., to appear in the *Proceedings of the Symposium on The Gerasimov-Drell-Hearn Sum Rule and the Spin Structure in the Resonance Region, 14-17 June 2000, Mainz, Germany.*
24. Low F.E., Phys. Rev. **110**, 974 (1958).
25. Guichon P.A.M., G.Q. Liu and A.W. Thomas, Nucl. Phys. **A591**, 606 (1995).
26. Drechsel D., G. Knöchlein, A. Metz, and S. Scherer, Phys. Rev. C **55**, 424 (1997).
27. Drechsel D., G. Knöchlein, A.Yu. Korchin, A. Metz, and S. Scherer, Phys. Rev. C **57**, 941 (1998).
28. Drechsel D., G. Knöchlein, A.Yu. Korchin, A. Metz, and S. Scherer, Phys. Rev. C **58**, 1751 (1998).
29. Vanderhaeghen Marc, Phys. Lett. B **402**, 243 (1997).
30. Vanderhaeghen Marc, Phys. Lett. B **368**, 13 (1996).
31. Roche J. et al., Phys. Rev. Lett. **85**, 708 (2000).
32. Bertin P.Y., P.A.M. Guichon and C. Hyde-Wright, spokespersons JLab experiment, E-93-050.
33. Shaw J. and R. Miskimen, spokespersons MIT-Bates experiment.
34. Pasquini B. and G. Salmè, Phys. Rev. C **57**, 2589 (1998).
35. Metz A. and D. Drechsel, Z. Phys. A **356**, 351 (1996); Z. Phys. A **359**, 165 (1997).
36. Hemmert T.R. and B.R. Holstein, G. Knöchlein and S. Scherer, Phys. Rev. Lett. **79**, 22 (1997).
37. Hemmert T.R., B.R. Holstein, G. Knöchlein, and D. Drechsel, Phys. Rev. D **62**, 014013 (2000).
38. d'Hose N. et al., Letter of Intent for MAMI experiment (1999).
39. Pasquini B., D. Drechsel, M. Gorchtein, A. Metz, and M. Vanderhaeghen, Phys. Rev. C **62** (2000) in press; hep-ph/0007144.
40. Vanderhaeghen M., D. Drechsel, M. Gorchtein, A. Metz, and B. Pasquini, to appear in the Proceedings of the Symposium on The Gerasimov-Drell-Hearn Sum Rule and the Spin Structure in the Resonance Region, 14-17 June 2000, Mainz, Germany.
41. Tarrach R., Nuovo Cimento A **28**, 409 (1975).
42. Drechsel D., O. Hanstein, S. Kamalov, L. Tiator, Nucl. Phys. A **645**, 145 (1999).
43. Drechsel D., M. Gorchtein, A. Metz, B. Pasquini, and M. Vanderhaeghen, in preparation.
44. Sterman G. and P. Stoler, Ann. Rev. Nucl. Part. Sci. **47**, 193 (1997).
45. Brodsky S.J. and G.P. Lepage, Phys. Rev. D **22**, 2157 (1980).
46. Chernyak V.L. and A.R. Zhitnitsky, Phys. Rep. **112**, 173 (1984).
47. Chernyak V.L., A.A. Ogloblin and I.R. Zhitnitskii, Z.Phys. **C42**, 569 (1989).
48. King I.D. and C.T. Sachrajda, Nucl. Phys. B **279**, 785 (1987).
49. Brodsky S.J. and G.R. Farrar, Phys. Rev. Lett. **31**, 1153 (1973).

50. Brodsky S.J. and G.P. Lepage, Phys. Rev. D **24**, 2848 (1981).
51. Sivers D., Phys. Rev. D **41**, 83 (1990).
52. Radyushkin A.V., Phys. Rev. D **58**, 114008 (1998).
53. Diehl M., T. Feldmann, R. Jakob, and P. Kroll, Eur. Phys. J. C **8**, 409 (1999).
54. Farrar G.R. and H. Zhang, Phys. Rev. D **41**, 3348 (1990); Phys. Rev. D **42**, 2413(E) (1990).
55. Farrar G.R., K. Huleihel and H. Zhang, Nucl. Phys. B **349**, 655 (1991).
56. Kronfeld A.S. and B. Nizic, Phys. Rev. D **44**, 3445 (1991); Phys. Rev. D **46**, 2272(E) (1992).
57. Vanderhaeghen M., P.A.M. Guichon, and J. Van de Wiele, Nucl. Phys. A **622**, 144c (1997).
58. Brooks T. and L. Dixon, hep-ph/0004143.
59. Wojtsekhowski B., A.M. Nathan, and C. Hyde-Wright, spokespersons JLab experiment E-99-114.
60. d'Hose N. and G. Tamas, in *Proceedings of the Workshop VCS'96*, edited by V. Breton, Clermont-Ferrand (1996).
61. D'Angelo A. et al., Nucl. Phys. A **622**, 226c (1997).
62. Ji X., Phys. Rev. Lett. **78**, 610 (1997); Phys. Rev. D **55**, 7114 (1997).
63. Radyushkin A.V., Phys. Lett. B **380**, 417 (1996).
64. Ji X., J. Phys. G **24**, 1181 (1998).
65. Watanabe K., Prog. Theor. Phys. **67**, 1834 (1982).
66. Bartels J. and Loewe M., Z. Phys. C **12**, 263 (1982).
67. Dittes F.M., Müller D., Robaschik D., Geyer B., and Horejsi J., Phys. Lett. B **209**, 325 (1988).
68. Jain P. and Ralston J.P., *Proceedings of the Workshop on Future Directions in Particle and Nuclear Physics at Multi-GeV Hadron Beam Facilities, BNL, New York* (1993).
69. Müller D., Robaschik, Geyer B., Dittes F.-M., and Horejsi J., Fortschr. Phys. **42**, 101 (1994).
70. Ji X. and J. Osborne, Phys. Rev. D **58**, 094018 (1998).
71. Collins J.C. and A. Freund, Phys. Rev. D **59**, 074009 (1999).
72. Vanderhaeghen M., P.A.M. Guichon, and M. Guidal, Phys. Rev. D **60**, 094017 (1999).
73. Radyushkin A.V., Phys. Rev. D **59**, 014030 (1998).
74. Martin A.D., R.G. Roberts, W.J. Stirling, R.S. Thorne, Eur. Phys. J. C **4**, 463 (1998).
75. Petrov V., P. Pobylitsa, M. Polyakov, I. Börnig, K. Goeke, and C. Weiss, Phys. Rev. D **57**, 4325 (1998).
76. Christov, Chr.V., A. Blotz, H.-C. Kim, P. Pobylitsa, T. Watabe, Th. Meissner, E. Ruiz Arriola, and K. Goeke, Prog. Part. Nucl. Phys. **37**, 91 (1996).
77. Polyakov M.V. and C. Weiss, Phys. Rev. D **60**, 114017 (1999).
78. Anikin I.A., B. Pire, and O.V. Teryaev, Phys. Rev. D **62**, 071501(R) (2000).
79. Penttinen M., M.V. Polyakov, A.G. Shuvaev, and M. Strikman, hep-ph/0006321.
80. Belitsky A.V., and D. Müller, hep-ph/0007031.
81. Diehl M., T. Gousset, B. Pire, J.P. Ralston, Phys. Lett. B **411**, 193 (1997).
82. Collins J.C., L. Frankfurt and M. Strikman, Phys. Rev. D **56**, 2982 (1997).
83. Radyushkin A.V., Phys. Lett. B **385**, 333 (1996).
84. Vanderhaeghen M., P.A.M. Guichon, and M. Guidal, Phys. Rev. Lett. **80**, 5064 (1998).
85. Mankiewicz L., G. Piller, T. Weigl, Eur. Phys. J. C **5**, 119 (1998).
86. Frankfurt L.L., P.V. Pobylitsa, M.V. Polyakov and M. Strikman, Phys. Rev. D **60**, 014010 (1999).
87. Mankiewicz L., G. Piller, T. Weigl, Phys. Rev. D **59**, 017501 (1999).
88. Mankiewicz L., G. Piller and A. Radyushkin, Eur. Phys. J. C **10**, 307 (1999).
89. Guidal M., C. Marchand, and E. Smith, spokespersons JLab experiment E-98-107/E-99-105.
90. Bertin P.Y., Y. Roblin and F. Sabatié, spokespersons JLab experiment, E-00-110.
91. Armarian M., private communication.
92. d'Hose N. et al., Letter of Intent for COMPASS experiment (1999).
93. Pochodzalla J., L. Mankiewicz, M. Moinester, G. Piller, A. Sandacz, and M. Vanderhaeghen; in Proceedings of the joint INT/JLab workshop Exclusive and semiexclusive processes at high momentum transfer, 20-22 May 1999, Jefferson Lab, Newport News, VA; hep-ph/9909534.
94. Schäfer T., and E.V. Shuryak, Rev. Mod. Phys. **70**, 323 (1998).
95. Adkins G., C. Nappi and E. Witten, Nucl. Phys. B **228**, 552 (1983).
96. Diakonov D.I., V.Y. Petrov and P.V. Pobylitsa, Nucl. Phys. B **306**, 809 (1988).
97. Frankfurt L.L., M. V. Polyakov, M. Strikman, and M. Vanderhaeghen, Phys. Rev. Lett. **84**, 2589 (2000).
98. Frankfurt L., W. Koepf and M. Strikman, Phys. Rev. D **54**, 3194 (1996).
99. Airapetian A. et al. (HERMES Collaboration), Eur. Phys. J. C (2000) in press; hep-ex/0004023.
100. Belitsky A.V., D. Müller, L. Niedermeier, A. Schäfer, Phys. Lett. B **437**, 160 (1998); Nucl. Phys. B **546**, 279 (1999).
101. Mankiewicz L., G. Piller, E. Stein, M. Väntinnen, T. Weigl, Phys. Lett. B **425**, 186 (1998).
102. Belitsky A.V., D. Müller, L. Niedermeier, A. Schäfer, Phys. Lett. B **474**, 163 (2000).
103. Bertin P.Y., Y. Roblin and C.E. Hyde-Wright; *Proceedings of the Conference of Nuclear and Particle Physics with CEBAF at Jefferson Lab*, Fiz. B, vol. 8 (1999) 2, 207.
104. Burkert V., M. Guidal, S. Stepanyan et al., to be published in the JLab 12 GeV upgrade "White Book", 2000.
105. Burkhardt H., (Editor) *Conceptual Design Report for ELFE at CERN*, CERN 99-10, 1999.
106. Vanderhaeghen M., J.M. Friedrich, D. Lhuillier, D. Marchand, L. Van Hoorebeke, and J. Van de Wiele, Phys. Rev. C **62**, 025501 (2000).